**The Bone Morphogenetic Pathway Controls the Uptake of Infectious Prions**

Elena De Cecco[1]*, Giovanni Mariutti[1], Carlos Omar Oueslati Morales[1], Davide Caredio[1], Hasier Eraña [2,3,4], Carolina Appleton[1], Stefano Sellitto[1], Simone Hornemann[1], Carlo Scialò[5], Jiang-An Yin[1], Enric Vidal[6], Magdalini Polymenidou[5], Joaquín Castilla[2,3,7] and Adriano Aguzzi[1]*

[1]Institute of Neuropathology, University of Zürich, CH-8091 Zürich, Switzerland.

[2]Center for Cooperative Research in Biosciences (CIC BioGUNE), Basque Research and Technology Alliance (BRTA), Derio, Spain.

[3]Centro de Investigación Biomédica en Red de Enfermedades infecciosas (CIBERINFEC), Carlos III National Health Institute, Madrid, Spain.

[4]ATLAS Molecular Pharma S. L., Derio, Spain.

[5]Department of Quantitative Biomedicine, University of Zürich, Zürich, Switzerland.

[6]IRTA. Programa de Sanitat Animal. Centre de Recerca en Sanitat Animal (CReSA). Campus de la Universitat Autònoma de Barcelona (UAB), Bellaterra, Catalonia. Spain.

[7]IKERBASQUE, Basque Foundation for Science, Bilbao, Spain.

* Correspondence to elena.dececco@uzh.ch or adriano.aguzzi@uzh.ch

**Abstract**

Prion diseases are transmissible neurodegenerative disorders caused by the spread of misfolded prion protein between cells and individuals, yet the paths by which prions colonize cells are undefined. Here we map the determinants of prion uptake with a genome-wide quadruple-guide CRISPR activation screen. Uptake of prions was measured by flow cytometry in *PRNP*-ablated human SHSY-5Y cells exposed to synthetic ovine prions. We identified 43 genes modulating prion uptake, 6 of which belonged to the core components of the Bone Morphogenetic Protein (BMP) signaling axis. Prion internalization was increased by overexpression of BMP receptors (BMPR1B, BMPR2, ACVRL1) and the Small Mothers Against Decapentaplegic (SMAD1 and SMAD5) intracellular BMP effectors, whereas the inhibitory SMAD6 reduced it. The internalization of other proteopathic seeds (α-synuclein, tau K18, amyloid-β) and other endocytic probes (transferrin, dextran, E. coli bioparticles) was unaffected. Transcriptional profiles of a panel of persistently prion-infected cell lines showed broad dysregulation of BMP-related signaling. Hence, BMP signaling is a gatekeeper of prion entry mechanistically distinct from bulk endocytosis and amyloid uptake. Chronic prion propagation induced SMAD1/5 phosphorylation, suggesting a positive-feedback loop during prion infection. The connection of prion uptake to a developmentally conserved morphogen pathway with rich pharmacology suggests that BMP signaling nodes may serve as tractable levers to modulate early events in prion transmission.

## Introduction

Prions consist of $PrP^{Sc}$, a misfolded and aggregated version of the normal cellular prion protein ($PrP^{C}$) which causes transmissible spongiform encephalopathies or prion diseases[1]. Prions primarily accumulate in the central nervous system, where they propagate from cell to cell along neuroanatomical pathways[2,3] ultimately triggering neuroinflammation[4], neuronal dysfunction[5] and cell death. Internalization of prions by susceptible cells represents a crucial initial step in establishing iatrogenic and alimentary prion infections such as variant Creutzfeldt-Jakob disease (vCJD[6]), and more generally because it is a precondition for the cell-to-cell spread of prions within affected organisms.

$PrP^{C}$ is co-translationally transferred to the lumen of the endoplasmic reticulum, where it acquires a glycophosphoinositol anchor tethering it to the external surface of biological membranes. While the conversion of $PrP^{C}$ to $PrP^{Sc}$ seems to take place mostly on the plasma membrane[7,8], prion deposits have been detected in components of the endolysosomal system including multivesicular bodies (MVBs), lysosomes and the endosome recycling compartments[9-13]. As $PrP^{C}$ is continuously recycled between vesicular compartments and the plasma membrane[14], these observations suggest that $PrP^{C}$ and $PrP^{Sc}$ follow, at least in part, converging trafficking routes[15].

Cell-type identity plays a major role in determining the modalities of prion entry. Within the gastrointestinal tract, specialized M cells and enterocytes transport prions from the gut lumen to the gut-associated lymphoid tissue (GALT), primarily via phagocytosis and endocytosis, delivering them to follicle-associated dendritic cells where initial replication events take place[16-19]. Transepithelial transport can occur in the absence of $PrP^{C}$ [16,20].

The diverse clinical outcomes of prion diseases have been linked to strain-specific patterns of cell tropism, which may be driven by variations in cellular entry routes and intracellular transport mechanisms[21]. $PrP^{Sc}$ may propagate from infected to healthy cells through various mechanisms, including direct cell-cell contact[22,23], tunneling nanotubes[24], exosomes[25], and transsynaptic passage[26-29]. Several proteins have been proposed to act as prion receptors[30-32] in cell lines and neurons, yet none was confirmed to be a valid target for antiprion therapies. It is plausible that yet unidentified pathways control prion pathogenesis by mediating prion uptake into cells, but their nature remains elusive. In most neurodegenerative diseases, the study of disease-associated genetic polymorphisms in humans has identified many modifiers of pathogenesis. With a few exceptions[33], however, this approach has proven mostly futile in prion diseases, and no other modifier except *PRNP* polymorphisms has been identified by human genetics.

CRISPR-based genetic screens, on the other hand, have proven to be a powerful methodology to uncover genes that modify scorable phenotypes – such as cellular features of disease. In contrast to the associative nature of GWAS, CRISPR approaches allow for direct functional interrogation and causal inference[34,35]. Here, we used a potent quadruple-guide (qgRNA) human CRISPR library[33] to conduct an unbiased CRISPR-activation screen of the entire human protein-coding genome, with

the aim to discover new pathways and cellular factors affecting transcellular prion spread. In addition to enumerating all genomic factors controlling colonization of cells by prions, we differentiate pathways affecting multiple proteopathic seeds from those private to prions.

## Results

### *Generation of a human cell line expressing a programmable transactivator*

The uptake of $PrP^{Sc}$ by susceptible cells is the initial step in the infection process. We modeled this process in the human neuroblastoma line SH-SY5Y, which is widely used in neurodegeneration research. Since internalization of $PrP^{Sc}$ was shown to occur also in the absence of $PrP^{C}$ expression[16,20], we eliminated $PrP^{C}$ expression by genetically ablating the *PRNP* gene[36] to prevent its potentially biohazardous conversion into human prions. Absence of $PrP^{C}$ also allows to investigate prion uptake without the confounding effect of replication.

For gene activation, we equipped cells with the programmable transactivator dCas9-VP64[37] (**Suppl. Fig. 1A**) which, in contrast to other transactivating proteins, did not adversely impact cell viability. To avoid loss of the transgene in the resulting polyclonal population, cells were kept under permanent antibiotic selection. *PRNP*$^{-/-}$ dCas9-VP64-expressing cells (henceforth termed SH-KO$^{vp64}$) showed strong genetic activation four days post transduction with quadruple CRISPR activation RNA guides (qgRNA)[33] targeting a randomly selected panel of genes (**Suppl. Fig. 1B – 1C**).

### *Exogenous synthetic prions are internalized by cells within 24 hours*

As a source of prions, we utilized synthetic ovine prions (ovPrP$^{Sc}$) produced by the in vitro aggregation of recombinant full-length ovine $PrP^{C}$ (VRQ genotype) using a modified Protein Misfolding Cyclic Amplification (PMCA) protocol known as PMSA (Protein Misfolding Shaking Amplification) in the presence of the cofactor dextran. Ovine $PrP^{C}$ shares 89.33% sequence identity with the human orthologous protein, and there is no evidence that the misfolded counterpart is capable of infecting humans[38,39], making it safer to handle (**Suppl. Fig. 2A**). These synthetic ovine prions, like other recombinant prions prepared using the same methodology[40], exhibited key characteristics of authentic prions: (i) heterogeneous fibrillar structures resembling brain-derived prion rods as observed by transmission electron microscopy (**Fig. 1A**), (ii) a 16 kDa PK-resistant fragment typical of PMSA-derived infectious prions (**Fig. 1B**) and (iii) 100% attack rates following intracerebral inoculation in TgVole (transgenic mouse line expressing bank vole PrP with I109 polymorphism) and Tg338 (overexpressing ovine VRQ PrP) (**Table 1**).

Prior to the uptake assay, ovPrP$^{Sc}$ aggregates were sonicated for 10 minutes in a high-power (~150 W and 40 kHz) water bath sonicator to fragment larger assemblies into smaller species, thereby

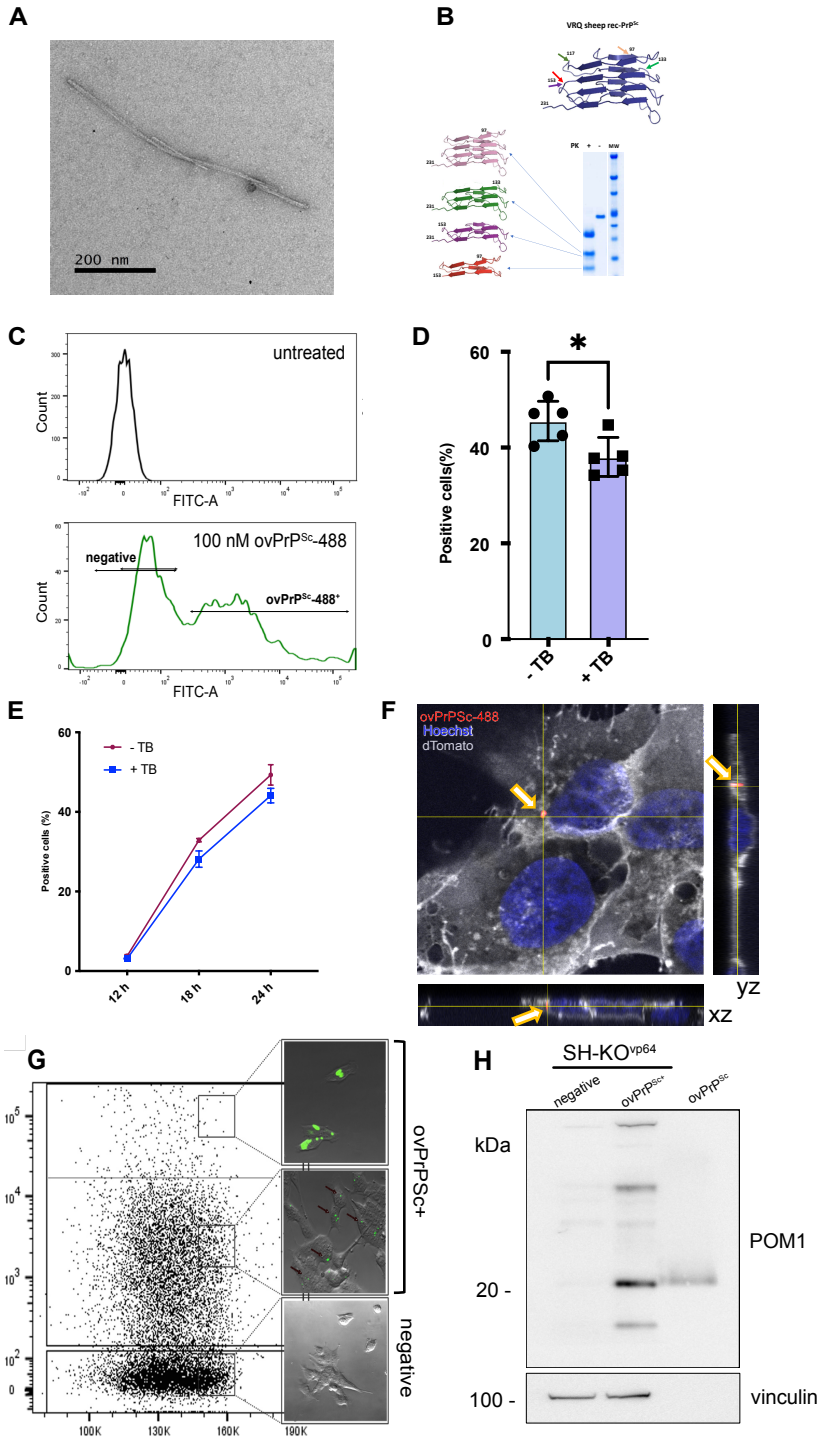


**Fig. 1. Prion uptake at single cell resolution. A**: Electron microscopy image of negatively stained ovine synthetic prion aggregates. **B.** Coomassie showing biochemical characterization of ovPrPSc upon digestion with proteinase K (PK). Cartoons show the distinct protein fragments corresponding to each band observed upon PK digestion. **C**: Histograms showing the distribution of untreated (grey curve) and ovPrP$^{Sc}$-488-treated (green curve) cells across the FITC channel. Peaks indicate the relative abundance of cells at each fluorescence level. **D.** Cells internalizing ovPrP$^{Sc}$-488 in the presence or absence of 2mM Trypan Blue (TB), which quenches fluorescence of non-internalized aggregates. Each dot represents one distinct experiment and is the average of two technical replicates. * = $p<0.05$, Student's T-test. **E.** Time-course kinetics of ovPrP$^{Sc}$-488 internalization in the presence or absence of 2mM TB. **F.** SH-KO$^{vp649}$ cells expressing farnesylated TdTomato treated with 100 nM ovPrP$^{Sc}$-488 (24 h). Orthogonal projections of z-stack images show internalized aggregates. **G.** ovPrPSc-488 treated SH-KO-dCas9 cells were sorted into three bins based on AlexaFluor-488 signals, replated, and imaged. Side panels: representative images of sorted cells. **H.** OvPrP$^{Sc+}$ cells and negative cells were sorted and analyzed via Western Blot. Purified ovPrP$^{Sc}$ was loaded as control.

| Inoculum | Mouse model | Passage | Attack rate | Incubation period (dpi ± SEM) | $PrP^{Sc}$ (WB) |
|---|---|---|---|---|---|
| $OvPrP^{Sc}$ | TgVole(I109)1x | 1st | 6/6 | 198 ± 26 | 6/6 |
| | Tg338 | 1st | 7/7 | 367 ± 15 | 7/7 |
| $OvPrP^{Sc}$>Tg338 | Tg338 | 2nd | 12/12* | 164 ± 17 | 12/12 |

**Table 1. Intracerebral** inoculation **of $ovPrP^{Sc}$ in TgVole and Tg338 mice.** *One mouse died of intercurrent disease and was not included in the calculations.

facilitating their internalization by cells. Density gradient centrifugation on 60% iodixanol showed that increasing fractions of $ovPrP^{Sc}$ aggregates were found in the supernatant fraction with longer sonication times, suggesting that long fibers had been fragmented (**Suppl. Fig. 2B**).

Next, prion aggregates were fluorescently labeled by conjugating succinimidyl ester of AlexaFluor488 to lysine residues to generate AF488-$ovPrP^{Sc}$. Upon flow cytometry, prion aggregates appeared as a broadly heterogeneous population, clearly distinct from live cells based on their lower FSC-A values (**Suppl. Fig. 3A**). $ovPrP^{Sc}$-488 aggregates showed a wide range of fluorescence intensities, possibly reflecting the broad size distribution of the sonicated prion preparation (**Suppl. Fig. 3B**). Incubation of SH-$KO^{vp64}$ cells with increasing concentrations of unlabelled or AF488-labelled $ovPrP^{Sc}$ did not affect overall cell survival and growth, as reflected by ATP levels assessed with CellTiter-Glo (**Suppl. Fig. 3C**).

We treated SH-$KO^{vp64}$ cells with $ovPrP^{Sc}$-488 (100 nM) added to the culture medium. After 24 hours, we trypsinized the cells to remove loosely adsorbed aggregates and performed flow cytometry analysis. (**Fig. 1C**). Fluorescence intensity in the FITC channel followed a bimodal distribution with two peaks, with one peak overlapping the untreated population and a second peak shifted toward higher fluorescence. This pattern indicates that only a subset of cells internalizes the aggregates. 45% ± 4.1% of the cell population showed high fluorescence intensity in the FITC channel, suggesting prion internalization. To test this, the same sample was reacquired in the presence of the amyloidophilic dye Trypan Blue[41] which quenches green fluorescence when present in solution[42] (**Fig. 1D, Suppl. Fig. 3B**). Despite a small (45% vs 38%, $p<0.05$) decrease in the prion positive cells in the presence of Trypan Blue, most cells (~ 85%) had internalized prions, indicating that unbound material had been removed. Overexpression of isogenic ovine $PrP^{C}$ resulted in a slight increase (16% ± 10%, $p<0.05$) in the percentage of $ovPrP^{Sc+}$ cells, suggesting that $PrP^{C}$ participates in the uptake of prions (**Suppl. Fig. 3D**).

Next, we assessed the kinetics of prion uptake over time. Consistent internalization was observed first after 18 hours of incubation and continued to increase over time (**Fig. 1E**). We chose 24 hours

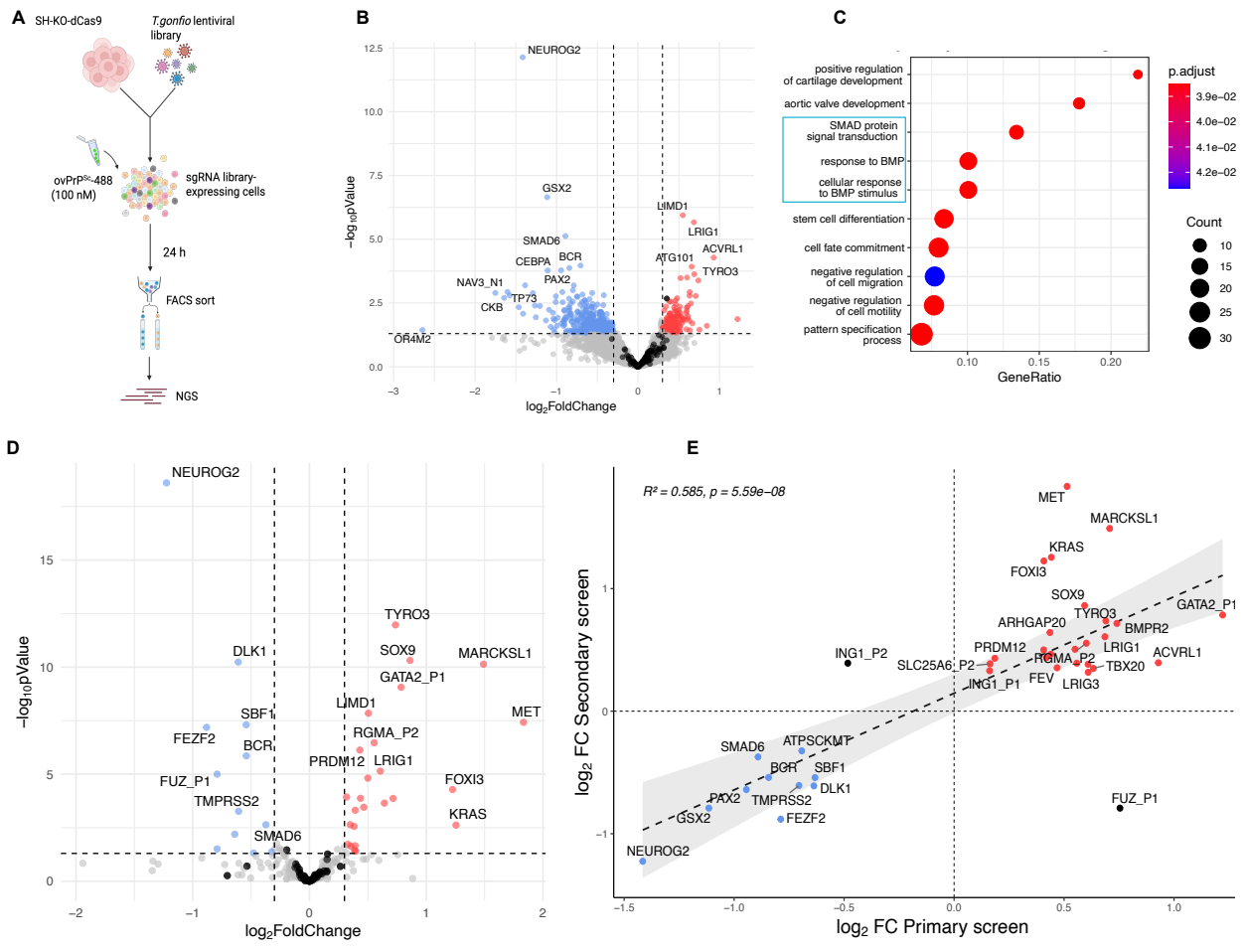


**Fig. 2. Genome-wide CRISPR activation screens for modifiers of prion uptake. A.** Screening workflow. **B.** Volcano plot showing enriched (red) and depleted (blue) qgRNA in ovPrP$^{Sc+}$ cells. Black dots: non-targeting qgRNA. Dotted lines: thresholding criteria ($log_2$ FC>±0.35, p-value <0.005). **C.** Overrepresentation of BMP-related genes among hits in three pathway enrichment analysis databases (REACTOME, KEGG and WikiPathways, visualized with gProfiler). **D.** Volcano plot showing a secondary screen of relevant genes. Color codes as in B. **E.** Correlation between primary and secondary screen for confirmed hits. X and Y axes: differential abundance between ovPrP$^{Sc}$+ and negative populations.

of incubation as ≈50% of cells had taken up prions at this time point. Confocal analyses of ovPrP$^{Sc}$-488-treated cells suggested that most aggregates resided within cell bodies (**Fig. 1F**). FACS sort of ovPrP$^{Sc}$-488-treated cells, followed by re-plating and microscopy analysis, showed the presence of larger dot-like fluorescent aggregates in the cell subpopulation exhibiting highest fluorescence intensity, whereas smaller dots decorated the cytoplasm of the lower-intensity subpopulation (**Fig. 1G**). The observed differences in the fluorescent signals could come from differently sized aggregates in the preparation or from labeling inhomogeneities. Alternatively, a fraction of cells might behave as "super-uptakers" and internalize more aggregates. Western blotting of the two sorted populations (ovPrP$^{Sc-}$ and ovPrP$^{Sc+}$) confirmed the enrichment of ovPrP$^{Sc}$ only in the prion-positive population (**Fig. 1H**). These findings show that prion uptake can be robustly modelled in human cell lines and that our experimental system is suitable for identifying prion uptake modulators through flow cytometry.

### *Genome-wide pooled CRISPR activation screen identifies 43 new modulators of prion uptake*

To identify genes involved in prion uptake, we conducted a whole-genome, FACS-based pooled CRISPR activation screen in SH-KO$^{vp64}$ cells (**Fig. 2A**). We used the "T.gonfio" human activation library which multiplexes four non-overlapping guides to enhance perturbation efficiency while minimizing off-target effects[33]. To eliminate template switch, lentiviral vectors were generated individually by plasmid transfection into helper cells and pooled in a second step to obtain the final library. SH-KO$^{vp64}$ cells were transduced with the lentiviral pool at a multiplicity of infection of 0.3, followed by puromycin selection for five days to remove unmodified cells. Six days after infection, SH-KO$^{vp64}$ were reseeded into multiple culture vessels and treated with ovPrP$^{Sc}$-488 (100 nM) for 24 hours. To ensure accurate population separation, cells located within the central, well-defined regions of the negative and positive peaks were isolated by FACS sorting and collected for genomic DNA extraction (**Suppl. Fig. 4A**). Post-sort reanalysis confirmed that both prion positive and prion negative populations were highly pure (**Suppl. Fig. 4B**). sgRNA distribution between positive and negative populations was analyzed by next-gen Illumina sequencing followed by enrichment analysis. The screen was performed in two independent replicates that showed excellent correlation, indicating robust technical performance (**Suppl. Fig. 4C**).

The primary hit list was selected with the following criteria: 1) normalized read count > 200 in both replicates; 2) p-value <0.05 as calculated from the two independent replicates; 3) $Log_2$ fold change > 0.3 or < -0.3 (**Fig. 2B, Supplementary Table 1**). Despite what shown in **Fig. S3D**, activation of the PRNP gene did not result in increased prion uptake ($log_2$FC: -0.002, p-value: 0.99), consistent with the absence of expression in the knockout background.
Among the most potent modifiers, we identified several genes known to participate in endocytic processes, such as the TAM receptor TYRO3[43] and the Ras-GTPase K-RAS[44], along with others that influence actin dynamics (i.e. MARCKSL1[45]). Identification of genes involved in cytoskeletal remodeling is consistent with an internalization-related phenotype, supporting the specificity and relevance of our assay.

Pathway analysis performed with ClusterProfiler revealed a strong enrichment of genes connected to the Bone Morphogenetic Protein (BMP) pathway and its downstream effectors (**Fig. 2C**). Core BMP components, including receptors and SMAD proteins, accounted for terms such as *"response to BMP"* and *"SMAD protein signal transduction"*. Additional morphogenetic gene ontology GO terms (e.g., *"cartilage development"*, *"aortic valve development"*) largely overlapped with these BMP genes, indicating a common signaling origin. Notably, all three LRIG (leucine-rich repeats and immunoglobulin-like domains) family members—LRIG1, LRIG2, and LRIG3—were among the hits; consistent with their reported regulation of BMP signaling, LRIG1 and LRIG3 acted as prion uptake promoters, whereas LRIG2 acted as a limiter**.** Collectively, these results suggest that the enriched

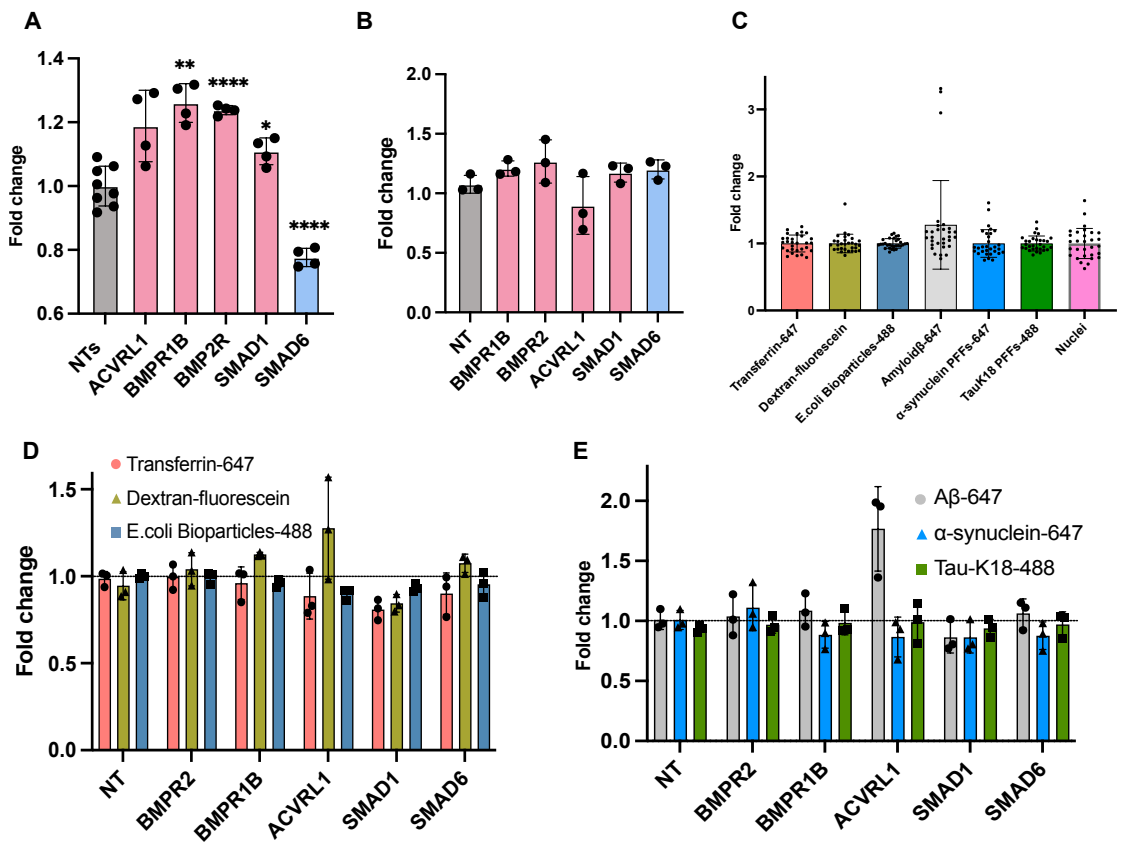


**Fig. 3. The BMP pathway controls prion internalization. A.** ovPrP$^{Sc}$-488 uptake upon genetic activation of individual BMP-related hit genes. NTs: pools of two non-targeting qgRNAs. **B.** Effect of BMP-related genes on cell growth (Hoechst-stained nuclei). Fold-change values relative to the mean of ten non-targeting controls, each assayed in triplicate (n = 30). **C.** Fold-change values for all 30 technical replicates of the non-targeting controls, calculated relative to the mean of the entire non-targeting control group, for all tested endocytic and neurodegeneration-related probes. Data illustrate the variability within and across the ten independent non-targeting conditions used for normalization in Fig. 3B–D-E. **D-E.** Effect of BMP-related genes on the uptake of endocytosis probes (D) and neurodegeneration-related protein aggregates (E). For legibility, a representative non-targeting condition is shown.

GO terms converge on a single biological axis — activation of the BMP/SMAD signaling module — which may modulate prion uptake in our cell model.

To refine candidate selection and eliminate false positives, we generated a library consisting of individually cloned lentiviral vectors encoding qgRNAs targeting 185 among the strongest candidate genes. Additionally, we included 70 non-targeting guides and 52 genes that did not score as hits to serve as internal controls, for a total of 368 plasmids. Individually generated lentiviruses were titrated, pooled and used to infect SH-KO$^{vp64}$ cells at a multiplicity of infection (MOI) of 0.3/cell. The secondary pooled screen was performed in three independent replicates at different days following the same workflow as in Fig. 2A. One of the three prion-positive samples was excluded due to poor DNA quality and the analysis was carried out using three and two replicates of the prion-negative and prion-positive conditions, respectively (**Suppl. Fig. 5A-B**). Out of 185 putative hits, 43 were confirmed in the secondary screen ($Log_2$ fold change >0.3 and < -0.3, p-value<0.05, **Fig. 2D, Suppl**.

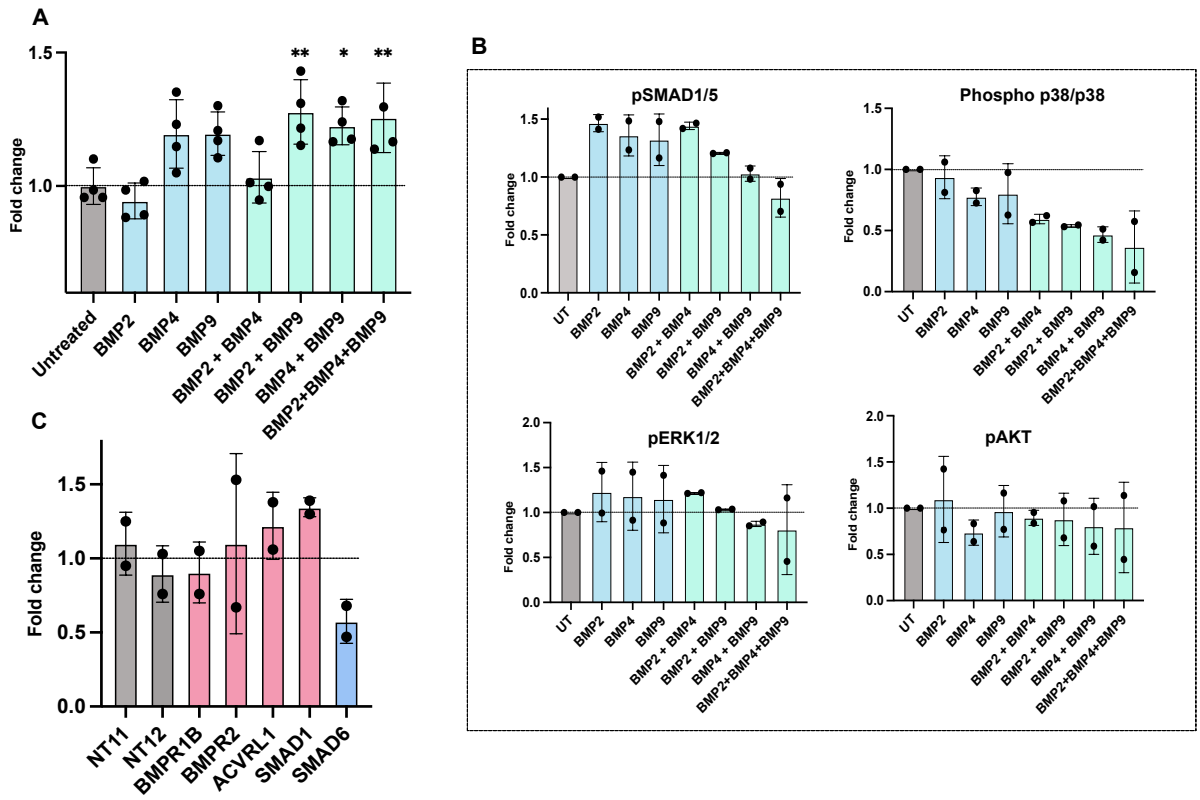


**Figure 4. A.** ovPrP$^{Sc}$-488 uptake upon treatment with 50 ng of BMP peptides added daily to the culture medium for 4 days. **B.** Western Blot quantification of canonical (pSMAD1/5) and non-canonical (pERK1/2, pAKT, phospho p38/p38) BMP downstream effectors. Vinculin: loading control. Dots: two biological replicates. All samples of each biological replicate were normalized to untreated controls (UT). **C.** Western Blot quantification of canonical (pSMAD1/5) BMP downstream effectors. Vinculin: loading control. Statistics in all panels: one-way Anova; Dunnett's post-hoc test.

**Table 2**). Confirmed hits showed a strong positive correlation ($R^2$ = 0.585) between primary and secondary screens, highlighting the consistency of the observed effects for these genes across independent experiments (**Fig. 2E**). Importantly, only two among all the non-targeting and non-hit guides passed our thresholding criteria and classified as false positives. This percentage falls within the bounds of statistical noise and therefore does not affect the reliability of the results. All genes associated with the core components of the BMP pathway were confirmed in the secondary screen, except for SMAD5 which only showed a subthreshold effect on prion uptake ($Log_2$ FC: 0.11, p-value:0.09). Chromosomal mapping revealed no shared promoters or close physical proximity among the identified hits, thereby excluding the possibility that their detection as hits resulted from concomitant activation of neighboring genes (**Suppl**. **Table 3, Suppl**. **Fig. 5C**).

### *Upregulation of BMP pathway members selectively affects prion uptake*

Prions can conceivably enter cells through specific receptors, by hijacking generic cellular endocytic pathways, or by a combination of mechanisms. We used CRISPR arrays to assess how the expression of individual BMP-related genes affected the uptake of prions and three types of particles known

to be internalized by cultured cells: transferrin (clathrin-mediated endocytosis), dextran 70 kDa (macropinocytosis) and E.coli bioparticles (phagocytosis).

Prion uptake was increased by overexpression of the two BMP receptors BMPR1B and BMPR2, and by overexpression of SMAD1, but decreased by SMAD6 overexpression (**Fig. 3A),** consistently with what was observed in the two screens. ACVRL1, a subtype of type-I receptors, showed a similar effect but did not reach statistical significance. Quantification of Hoechst-stained nuclei revealed no impact on cell growth and viability upon their genetic overexpression (**Fig. 3B**). Interestingly, none of the tested BMP-associated genes seemed to regulate the internalization of other endocytic probes (**Fig. 3C-D, Suppl. Fig. 6A**). Given the substantial differences in size and biochemical properties between endocytic probes and protein fibrils, we further assessed the hit genes using a panel of in vitro aggregates associated with neurodegeneration—including α-synuclein, tau K18, and amyloid-β fibrils—which all share a highly enriched β-sheet structure with prions. Again, overexpression of BMP proteins did not result in any detectable change in fibril uptake (**Fig. 3D-E, Suppl. Fig. 6A**). We extended our investigation to other confirmed hit genes (**Suppl. Fig. 6B, 6C, Suppl. Tables 4-5**). While most of the genes did not affect any endocytic pathways, a few candidates led to increased uptake of all protein fibrils (**Suppl. Fig. 6C**). In contrast to KRAS, which enhanced the uptake of all tested protein fibrils, TYRO3 selectively increased the internalization of synuclein fibrils ($\log_2$FC 0.53, p-value < 0.05), suggesting size-dependent selectivity or a more specific interaction with these proteins. Notably, the prion uptake enhancer FOXI3, a transcription factor belonging to the family of forkhead box (FOX) proteins, strongly increased uptake of all fibrils but showed no effect on non-aggregated probes, independently of their size.

### *Relationship between BMP activity and prion uptake*

We reasoned that increased prion uptake could either result from direct interaction between receptors and aggregates or could be induced by downstream effectors of BMP pathway activation. Indeed, despite the absence of BMP ligands in our final hit list, pathway activation could still occur as genetic upregulation of individual BMP components could promote ligand-independent activation of the pathway by spontaneous receptor oligomerization or SMAD autophosphorylation. To test this latter hypothesis, we first activated the BMP pathway by treating SH-KO$^{vp64}$ cells with three BMP peptides (BMP2, BMP4, BMP9, alone and in combination) for 4 days and quantified prion uptake (**Fig. 4A**). Samples treated with combinations of the three peptides showed enhanced prion entry compared to the untreated control, except for the combination of BMP2 and BMP4 which had no effect.

Different BMP peptides are reported to trigger specific downstream pathways, although the nature of the response depends on the target cells. We assessed the levels of phosphorylated SMAD1/5 (pSMAD1/5, canonical signaling pathway) as well as other non-canonical downstream effectors

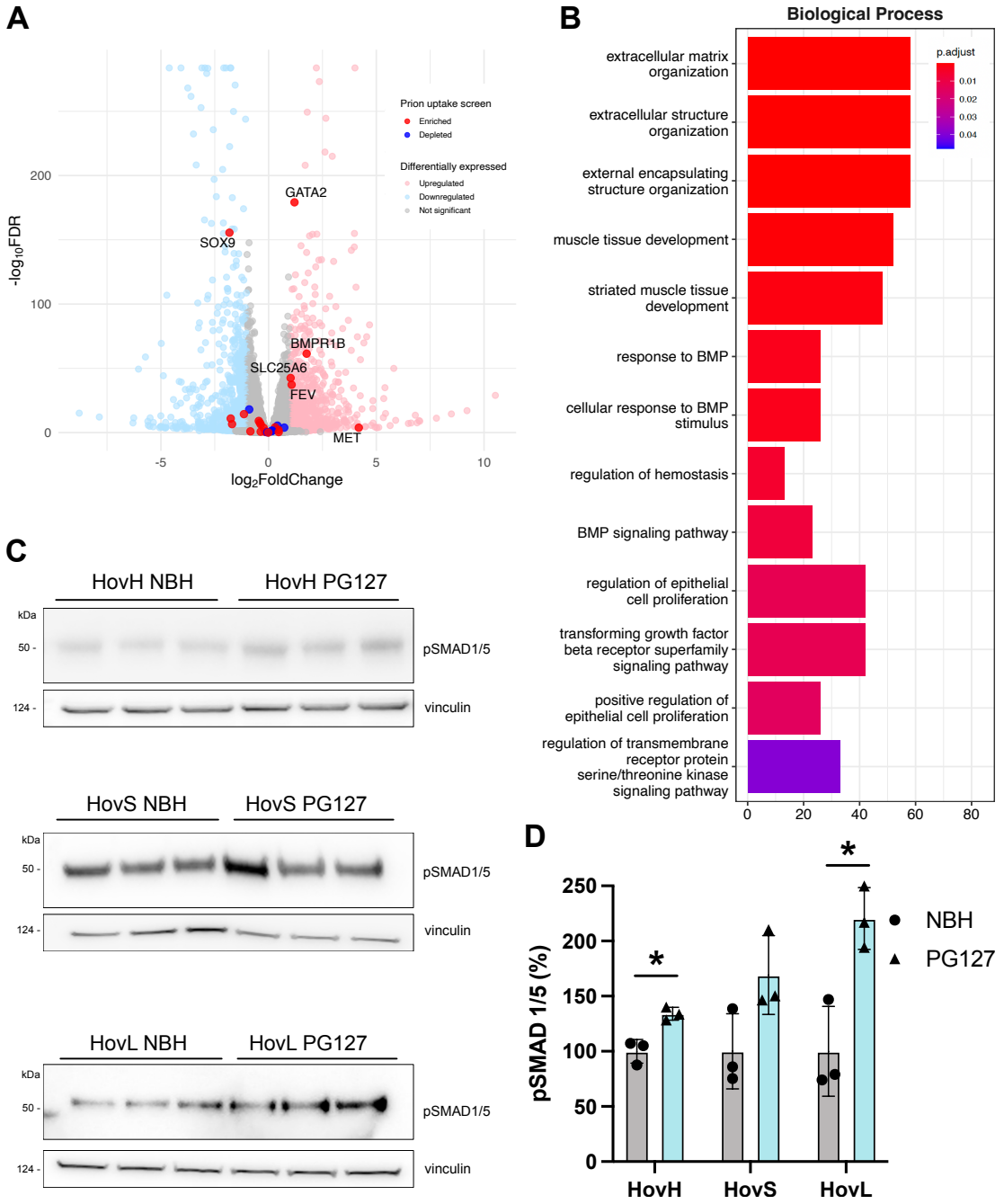


**Fig. 5. A.** DEGs in prion-infected vs. NBH-treated HovS cells. Highlighted genes denote those that also modulate prion uptake. Colors of highlighted genes indicate their effect on prion uptake according to the screnn data (red dot: uptake enhancers; blue dot: uptake limiter). **B.** Gene-ontology analysis reveals enrichment of four BMP-related GO terms consistently across the DEG datasets of HovS cells. **C.** Western Blots show cellular levels of phosphorylated SMAD1/5 in prion-infected and mock-infected HovH, HovS and HovL lines. **D.** Quantification of the Western Blots shown in C.

(phosphorylated ERK1/2, phosphorylated p38, phosphorylated AKT) (**Fig. 4B, Suppl. Fig. 7**). However, we did not detect any clear increase in the levels of phosphorylated markers. Levels of pSMAD1/5 increased following treatment with individual BMPs and with the combined application of two of the peptides but decreased when all three peptides were applied simultaneously. While phosphorylated ERK1/2 and phosphorylated AKT fluctuated around baseline levels, we observed a sharp

decrease in the ratio between phosphorylated p38 and total p38 in presence of two or more BMP peptides, indicating that the MAPK signaling pathway is being shut down.

We next investigated whether the canonical, pSMAD-dependent signaling pathway was activated upon genetic upregulation of BMP core components. Western blot analysis showed no substantial increase in pSMAD1/5 levels across most conditions, except for SMAD1 upregulation, which led to a modest rise in its phosphorylated (active) form (**Fig. 4C)**. In contrast, overexpression of SMAD6 led to reduced pSMAD1/5 levels, consistent with its known function as a BMP signal inhibitor.

### *BMP-associated genes are dysregulated in prion-infected cell lines*

We next asked whether any of the identified hits exhibit transcriptomic alterations in cellular models of prion infection. To this aim, we extracted total RNA from our scrapie-susceptible, low-biohazard human cell line (HovS)[46] infected with either non-infectious (NBH) or PG127-infected murine brain homogenates and performed bulk RNA sequencing. Differentially Expressed Gene (DEG) analysis revealed that out of 43 confirmed hit genes, 11 were significantly (log2FC> 1 and < -1; FDR<0.05) dysregulated in prion propagating cells compared to the control condition (**Fig. 5A**). Interestingly, 4 out of 11 DEGs were either core components (SMAD6, BMPR1B) or known downstream effectors of the BMP pathway (GATA2, SOX9). Moreover, Gene Ontology analysis on the complete list of DEGs showed that four GO terms related to the BMP pathway were significantly enriched (FDR<0.05) in our dataset (**Fig. 5B**). Since HovS cells originate from the same SH-SY5Y *PRNP* knockout line used in this study, we considered that the prion-induced dysregulation of the BMP pathway may reflect a cell line–specific effect rather than a generalizable response to infection. Therefore, we ovinized two additional cell lines of distinct origin: the embryonic kidney–derived HEK293A (termed HovH) and the glioblastoma-derived LN229[47] (termed HovL). Bulk RNA sequencing followed by Gene Ontology analysis confirmed a significant enrichment of BMP-related genes among the differentially expressed genes in response to infection with the PG127 prion strain in these two lines (**Suppl. Fig. 8A-B**). The overlap between the differentially expressed genes and our candidate list yielded only three shared genes per cell line (BMPR1B, GATA2 and RGMA for LN229; BMPR2, SLC25A6 and PAX2 for HEK293A), which is not unexpected given the distinct lineage of these cells compared to SH-SY5Y. Of note, all shared genes except for SLC25A6 were functionally linked to the BMP pathway, with RGMA being a membrane co-receptor and the transcription factors GATA2 and PAX2 acting downstream of BMP signaling[48-52]. Consistently with its dysregulation only in HEK293A-derived cells, PAX2 has been reported to respond to BMP signaling exclusively in kidney cells[53].

We next examined whether the transcriptional changes observed in BMP pathway components impacted activation of its canonical downstream signaling cascade. Prion-infected lines showed a small but consistent increase in the levels of phosphorylated SMAD1/5 compared to mock-infected controls (**Fig. 5C-D, Suppl. Fig. 9**), indicative of dysregulated pathway activity. Collectively, these

findings suggest a role for the BMP pathway and its downstream effectors in supporting the maintenance of stable prion infection. Notably, this effect appears to be conserved across cell lines of distinct origin, highlighting a potentially generalizable mechanism.

**Discussion**

In many ways, prions behave similarly to viruses: they enter cells, hijack biological processes for their own replication, exfiltrate themselves and eventually infect other cells and even other individuals. Quantitative assays can be devised to investigate each of these steps in the prion life cycle. Here, we set out to identify the molecular levers that control prion uptake by cells – the initial step required for the establishment and persistence of prion infections. Unlike $\alpha$-synuclein and tau fibrils, for which several receptors and facilitators have been described in human systems[54-61], little is known about the molecules engaging with prions at the cellular surface – let alone the genetic network controlling their activity

CRISPR-based screening interrogates the entire genome without relying on prior assumptions, thereby identifying unexpected and novel pathways that might otherwise be overlooked. We employed an upregulation-based genetic approach that allows targeting of genes with low basal expression as well as redundant and compensatory pathways. To achieve this, we created a pooled format of our next-generation human CRISPRa arrayed library (T.gonfio)[33] by separately packaging each plasmid into lentiviral particles and subsequently combining them into a single pool. This approach eliminates the problem of template switching which arises during lentiviral packaging of pooled plasmid libraries, while preserving the strong activation effects conferred by the quadruple sgRNA design.

The ultimate goal of prion research is the development of therapies – which typically requires validation of genetic findings in human systems. However, human prions are dangerous agents, and biosafety is a major concern. We addressed this with two complementary strategies. Firstly, we engineered the human neuroblastoma line SH-SY5Y and knocked out the endogenous prion protein, whose expression is necessary and sufficient for prion replication. In addition to reducing biohazards, ablation of *PRNP* did not affect the prion internalization process, hence enabling the study of the prion uptake process in an isolated manner, unconfounded by prion replication. Secondly, we treated SH-SY5Y cells with pure preparations of recombinant ovine $PrP^{Sc}$ (VRQ) generated through misfolding of the monomeric protein via iterative shaking cycles in the presence of the co-factor dextran. While the resulting aggregates showed infectivity in transgenic animals, establishing them as genuine, infectious prion species [40,62], epidemiological data have never uncovered any correlation between the consumption of food from scrapie-infested sheep flocks and human prion diseases. Hence, we deem sheep prions to be less dangerous to humans than bovine and human prions.

SH-SY5Y cells efficiently internalized $ovPrP^{Sc}$, although more slowly than what described for other prionoids in similar lines. This difference in kinetics may be attributable to the relatively large size of

our prion preparations[63], which contain aggregates several hundred nanometers in length. Although sonication increased the buoyancy of the preparation—indicating that some degree of fragmentation occurred—the fibrils may have nevertheless remained quite large. Hence, we settled opted for a 24-hour treatment paradigm which allowed consistent internalization. Despite not being necessary for the uptake, $PrP^C$ on the cell membrane slightly increased the amount of internalized prions. Several studies have highlighted a role for $PrP^C$ in the internalization and downstream toxicity of neurodegeneration-related amyloids[55,60,64-67]. Our results extend this paradigm to the uptake of infectious prions and suggest that $PrP^C$ might be involved in all steps of prion infection, beyond its established role in replication and toxicity.

Interrogation of the entire protein-coding genome by CRISPR activation pointed to 43 genes whose upregulation affected prion uptake. Most of these genes had not been previously linked to neurodegenerative diseases, indicating that genome-wide functional genomics investigations can powerfully complement human genetics studies. According to the available functional annotations, 32 (71%) of the identified modifiers encode either membrane-associated proteins or transcription factors. The prevalence of these functional classes of proteins is not unexpected. Transcription factors coordinate the expression of many effectors often contributing to synergistic functions, suggesting that prion uptake involves coordinated transcriptional programs. Conversely, the overrepresentation of membrane proteins points to their possible roles in the recognition, binding and internalization of prions, or alternatively in triggering signal transduction pathways that modulate prion entry. This observation implies that prion entry is governed by an intricate interplay between surface-level interactions and transcriptionally mediated cellular states, underscoring the complexity of the early stages of prion pathogenesis.

Among the strongest enhancers of prion uptake, we identified several modulators of macropinocytosis (K-RAS)[68] and phagocytosis (TYRO3)[69,70], along with modulators of actin dynamics like MARCKSL1[45]. Interestingly, TYRO3 is the only member of the TAM receptor family to be highly expressed in the central nervous system, and specifically in neurons[71,72], where it promotes the maturation of glutamatergic synapses[73]. While TYRO3 normally requires binding of its ligands (GAS6 and Protein S)[74] to dimerize and become active, we found that its overexpression alone sufficed to promote the accumulation of prions and internalization of E. coli particles. The apparent ligand-independent activation of TYRO3 may be attributable to the transcription-enhancing potency of the quadruple-guide-mediated upregulation. Indeed, increased levels of TYRO3 on the membrane might result in spontaneous dimerization and subsequent activation, hence leading to increased uptake. Similarly, the membrane-associated protein MARCKSL1 is known to regulate the formation of phagosomes[75] through its effects on actin filaments polymerization. A recent study highlighted the complex interplay between MARCKSL1 and the cellular prion protein, which appears to regulate MARCKSL1 stability[76]. Although $PrP^C$ ablation is expected to reduce MARCKSL1 stability, upregulating MARCKSL1 via our CRISPR qgRNAs may counteract this instability, enabling us to assess its

impact on prion uptake. These findings align with previous studies[43,77,78] and indicate that a subset of prions may enter cells via non-specific, phagocytosis-like pathways.

Gene ontology analysis showed a significant enrichment of BMP signaling–related genes in the prion-positive population. Bone Morphogenetic Proteins (BMPs), their receptors and downstream effectors are members of the TGF-β superfamily that regulate key processes such as cell growth, differentiation, and tissue homeostasis[79,80]. They signal primarily through the SMAD1/5/8 intracellular transducers[81-84] but can also activate multiple non-canonical pathways—such as phosphoinositol signaling (PI3K/Akt), tyrosine kinases (MAPK) and Rho-GTPases—depending on cellular context, receptors composition and pathway crosstalk[85]. We observed a strong enrichment in the prion positive population of core components of the pathway — such as the receptors BMPR1B, BMPR2, and ACVRL1, the SMAD proteins SMAD1, SMAD5; the co-receptor RGMA, and as several transcription factors regulated by SMAD-mediated signaling. Most interestingly, SMAD6, which is a negative regulator of BMP signaling, was enriched in the prion-negative cells. The bidirectional control of prion entry by positive and negative BMP signals provides strong evidence for the biological relevance of this finding.

The absence of many BMP ligands among our screen hits is unsurprising in view of their non–cell-autonomous function. Like all secreted signals, BMP ligands act on receiver cells distinct from the cells in which they are produced. This makes it impossible to select the cells expressing BMP ligands in immunofluoresence-based pooled screens, thereby preventing their detection. In contrast, overexpression of cell-autonomous components such as BMP receptors or SMADs activates downstream signaling within the same cell[86,87], allowing for their selection and detection in pooled screens.

Enrichment in BMP core components and downstream effectors was reflected in GO terms such as “response to BMP”, “cellular response to BMP stimulus” and “SMAD protein signal transduction”. Additional morphogenetic terms (e.g., “positive regulation of cartilage development”, “aortic valve development”, and “formation of primary germ layer”) largely overlapped with BMP core genes, with additional process-specific genes included in each term. Within our model system, these morphogenetic terms likely reflect the engagement of general BMP-induced developmental and differentiation pathways, which typically involve cytoskeletal remodeling and membrane trafficking, and may contribute to the observed phenotype. Taken together, these results support the idea that canonical BMP signaling actively promotes prion internalization. This is in line with recent reports that linked dysfunctions in the BMP pathway with Alzheimer’s Disease[88,89] and Amyotrophic Lateral Sclerosis[88,89], with increased BMP signaling activity leading to cell damage, aggregates’ deposition and toxicity. However, we did not observe any changes the uptake of non-aggregated endocytic probes or of fibrillar aggregates of other neurodegeneration-associated proteins, suggesting that at least in our model, the BMP pathway is acting specifically on prions.

Chronic pharmacological stimulation of the BMP pathway with recombinant BMPs recapitulated the observed increase in prion uptake, although the effect varied across distinct BMPs. Specifically, BMP9 had the strongest effect both alone and in combination with the other ligands, whereas BMP2 failed to do so. Treatment with BMPs has been shown to shift neuroblastoma lines towards a differentiated phenotype, marked by reduced proliferation and cell cycle exit[90-92]. BMP9 in particular was reported to direct cells towards a cholinergic state through Smad-mediated and Akt-mediated signaling[93]. Combined with our observations, this highlights a potential link between neuronal subtype identity and enhanced prion internalization, a relationship that warrants further investigation. Unexpectedly, activation of canonical downstream effectors (pSMAD1/5, pERK1/2, pAKT, phospho p38/p38) did not correlate with enhanced prion uptake, with phospho p38/p38 even showing an opposite trend. This may reflect negative feedback during prolonged high-dose BMP stimulation: signaling peaks early and then declines, while transcriptional programs persist for days, driving increased prion entry. Consistently, several hit genes encode transcription factors known to respond to BMP activation. In contrast, CRISPRa-mediated activation of BMP receptors and SMAD effectors produced sustained pSMAD1/5 signaling, suggesting that differences in activation method can influence signal dynamics, though in both cases transcriptional changes likely underlie the phenotype.

Consistently, persistently prion-infected cells showed altered expression of several BMP components compared to mock-infected controls. This effect was observed in both brain- and kidney-derived cell lines, suggesting that the dysregulation represents a general mechanism rather than a cell type–specific response. Experimental validation confirmed differences in the transcriptomic profiles across all three cell lines, each displaying increased activation of the BMP pathway, at least through the SMAD-dependent canonical signaling route. Elevated pathway activity in infected cells may therefore facilitate both the initial uptake of prions into naïve cells and the maintenance of persistent infection, potentially contributing to propagation across tissues.

The genome-wide association study by Jones and colleagues[94] identified several risk loci for sporadic Creutzfeldt–Jakob disease (sCJD), including *STX6*, *GAL3ST1*, and *PDIA4*, but left open the question of how these genes relate to prion pathogenesis. Interestingly, three of our hit genes mapped to genomic regions identified as risk factors for sCJD (BMPR2, p-value = 0.0019; MECOM, p-value = 0.034; SOX7, p-value = 0.047), and a fourth hit was just below the threshold (LRIG1, p-value = 0.051). Among them, SOX7 and LRIG1 have been shown to participate and/or regulate the BMP signaling pathway. SOX7 is a transcription factor that has been shown to modulate BMP2 signaling during cardiovascular development[95,96], while LRIG1 increase SMAD phosphorylation by directly binding BMP receptors[97]. The transcription factor MECOM is mostly involved in cell cycle regulation, but a recent report highlighted its interplay with several well conserved signaling pathways, including the TGF-β and BMP pathways[98]. Together, the convergence of these sCJD-associated genes on the BMP axis suggests a possible mechanistic link between prion disease susceptibility and dysregulation of BMP-related signaling processes.

In conclusion, we identify the BMP pathway as a key regulator of prion uptake in human cells. Genetic upregulation of core BMP components enhanced prion internalization, likely via ligand-independent pathway activation and downstream transcriptional effects. These findings reveal that prion entry is governed by more than simple endocytic processes. While our experiments focus on a single step of prion spread with naked prions, they align with observations in persistently infected cells, suggesting a broader, cell type–independent mechanism. Our results provide a rationale for targeting BMP signaling to modulate prion uptake and propagation in human cells and in disease contexts.

## Materials and methods

### *Cell culture*

SHSY5Y PRNP KO cells were generated as described in[36]. Cells were cultured in OptiMEM (Gibco, 11058021) supplemented with 10% fetal bovine serum (FBS) (Clontech Laboratories) and 1% penicillin/streptomycin (P/S) (Gibco, 15140122). The HEK-293T cell line for lentivirus production was cultured in DMEM (Gibco, 41965039) supplemented with 10% FBS. For lentiviral delivery, SHSY5Y cells were seeded in antibiotic-free OptiMEM, transduced in antibiotic-free OptiMEM supplemented with Polybrene 8 mg/mL (Millipore, TR-1003-G) and placed under antibiotic selection 24 hours after transduction. All cells were maintained in culture at 37 °C in a 3% oxygen and 5% CO2 atmosphere. For cells expressing farnesylated dTomato (used in Fig. 1F), the plasmid was a courtesy of Dr. Nikole Zuniga Qiuroz and Dr. Esther Stoeckli[99]. Plasmid was packaged in a lentiviral construct and used to transduce SH-KO$^{vp64}$ cells. Transduced cells were kept under antibiotic selection (geneticin, 0.4 mg/mL) until a stable line was established.

### *Lentivirus production*

All the lentiviral vectors were produced as follows: HEK-293T cells were seeded at 70% confluency, and 24 hours later the transfer plasmid containing the sequence of interest was co-transfected together with the pCMV-VSV-G (Addgene plasmid # 8454) and psPAX2 plasmids (Addgene plasmid #12260) using Lipofectamine 3000 transfection reagent (Invitrogen). After 6 hours, the medium was replaced with DMEM supplemented with 10% FBS and 1% HyClone Bovine Serum Albumin (Cytiva). 72 hours after transfection, supernatant was collected, aliquoted and stored at -80°C. To measure viral titer, SHSY5Y were seeded in 24-well plates at the final density of 100’000 cells/well. Lentiviral delivery was performed the day after seeding following culture conditions described above. At 72 hours from infection, expression of the BFP selection marker encoded by the transfer plasmid was measured by flow cytometry using the LSRFortessa Flow Cytometer (BD Biosciences). Data were evaluated with FlowJo 10 (Tree Star) to determine the percentage of fluorescent cells and to calculate the titer according to the following formula: Titer = (P*N)/V. P = percentage of BFP-positive cells; N = number of cells at the time of infection; V = volume of virus added.

### *Recombinant prion protein expression and purification*

The recombinant prion protein corresponding to sheep (Ovis aries) VRQ polymorphic variant (amino acids 23-231) (Accession number: AJ000738) was produced based on previously published protocols with extensive detail on protein production and purification[40]. Briefly, the Ovis aries PRNP gene encoding the VRQ variant was cloned into pOPIN E expression vector (Oxford Protein Production Facility) using standard molecular biology techniques. Escherichia coli Rosetta (DE3) competent cells (EMD Millipore) were transformed with the vector and cultured in LB medium supplemented with 50 µg/ml ampicillin at 37°C with vigorous agitation. Protein expression was induced by adding

isopropyl β-D-1-thiogalactopyranoside (IPTG) to a final concentration of 1 mM when the bacterial culture reached appropriate optical density. After 3 hours of induction, the bacterial cultures were harvested by centrifugation at 4,500 g for 15 minutes at 4°C.

Bacterial pellets were resuspended in lysis buffer (50 mM Tris-HCl pH 8, 5 mM EDTA, 1% Triton X-100, 1 mM PMSF) containing 100 µg/ml lysozyme. The suspension was treated with 100 U/ml DNase and 20 mM $MgCl_2$ for 30 minutes at room temperature with gentle agitation. Following centrifugation at 8,500 g for 1 hour at 4°C, the inclusion bodies containing the recombinant protein were collected. These were washed with 20 mM Tris-HCl, 150 mM NaCl, 1 mM EDTA, 1% Sarkosyl, pH 8, and solubilized overnight in 20 mM Tris-HCl, 0.5 M NaCl, and 6 M guanidine hydrochloride (GdnHCl), pH 8, at 37°C with vigorous shaking.

The solubilized sheep VRQ rec-PrP was purified using histidine affinity chromatography with a HisTrap FF crude 5 ml column (GE Healthcare) connected to an ÄKTA Start FPLC system. Purification was performed by taking advantage of the natural histidine residues in the octapeptide repeat region of PrP. The column was washed with binding buffer (20 mM Tris-HCl, 500 mM NaCl, 2 M GdnHCl, 5 mM imidazole, pH 8) and the protein was eluted with elution buffer (20 mM Tris-HCl, 500 mM NaCl, 500 mM imidazole, 2 M GdnHCl, pH 8). After elution, GdnHCl concentration was increased to 6 M for long-term storage. Protein quality and purity were assessed by BlueSafe (NZYtech) staining after electrophoresis in SDS-PAGE gels. The concentration was adjusted to 25 mg/ml using 10 kDa centrifugal filter units (Amicon Ultra-15, Millipore) and the purified sheep VRQ rec-PrP was stored at -80°C until use.

### *Substrate preparation for Protein Misfolding Shaking Amplification*

The PMSA substrate containing sheep VRQ rec-PrP was prepared following protocols adapted from previous studies[100]. In brief, the purified rec-PrP stored in 6 M GdnHCl was thawed and diluted 1:5 in phosphate-buffered saline (PBS, HyClone) to facilitate refolding through dialysis. The diluted protein solution was dialyzed against PBS at a 1:10,000 ratio for 1 hour at room temperature to promote proper folding of the protein. Following dialysis, the sample was centrifuged at 19,000 g for 15 minutes at 4°C to remove any aggregates formed by improperly folded proteins.

The concentration of the dialyzed sheep VRQ rec-PrP in the supernatant was determined using a bicinchoninic acid (BCA) protein assay kit (Thermo Scientific) and adjusted to achieve a final concentration of 2 µM (approximately 0.1 mg/ml) in the complete substrate. The protein solution was then mixed with conversion buffer (CB: PBS containing 0.15 M NaCl and 1% Triton X-100) at a 1:9 ratio. For experiments requiring cofactor-supplemented substrate, dextran sulfate sodium salt (molecular weight 6,500-10,000 Da, Sigma-Aldrich) was added to a final concentration of 0.5% (w/v). For cofactor-free experiments, the substrate was prepared identically but omitting dextran sulfate.

The final substrate preparations were aliquoted into appropriate volumes to minimize freeze-thaw cycles and stored at -80°C until required for PMSA experiments. Prior to each experiment, substrate quality was verified by electrophoresis and total protein staining to ensure consistent protein concentration and the absence of degradation products.

### *$PrP^{Sc}$ detection by electrophoresis and Western blot*

Proteinase K digestion of brain homogenate samples: For PrPSc detection in brain homogenates from inoculated animals, PK (Roche) digestion was performed prior to Western blotting. Previously homogenized brains of inoculated animals [at 10 % (w/v) in PBS (Fisher Bioreagents) with Protease inhibitor cocktail (Roche)] were mixed with digestion buffer [2 % (w/V Tween-20 (Sigma-Aldrich), 2 % (v/v) NP-40 (Sigma-Aldrich) and 5 % (w/v) Sarkosyl (Sigma-Aldrich) in PBS] at 1:1 (v/v). PK was added to reach a final concentration of 170 µg/ml in each sample, which were incubated at 42 ˚C for 1 h with shaking at 450 rpm in a thermomixer (Eppendorf). Digestion was stopped by adding loading buffer (NuPage 4x Loading Buffer, Invitrogen Life Technologies) 1:3 (v/v) and boiling samples for 10 min at 100 ˚C.

Western blot: Digested samples, together with non-digested controls, were boiled at 100 °C for 10 min and loaded onto 4-12 % acrylamide gels (NuPAGE Midi gel, Invitrogen Life Technologies) for 1 h 20 min (10 min at 70 V, 10 min at 110 V and 1 h at 150 V). Samples were then transferred to PVDF membranes using the iBlotTM 3 (Invitrogen Life Technologies). The membranes were developed using the iBindTM Flex Western Device (Invitrogen Life Technologies) and Sha31 (1:4,000) monoclonal antibody (Cayman chemical). After incubation with peroxidase-conjugated secondary anti-mouse antibody (m-IgGκ BP-HRP, Santa Cruz Biotechnology), membranes were developed with an enhanced chemiluminescent horseradish peroxidase substrate (West Pico Plus, Thermo Scientific). An iBrightTM CL750 imaging system (Invitrogen Life Technologies) was used for image acquisition and the software AlphaView (Alpha Innotech) for image processing.

### *Ethics Statement*

TgVole (1x) founder mice were generated at Transgenic Facility of the University of Salamanca (Spain) and breeding colonies were kept on a 12:12 light/dark cycle, receiving food and water ad libitum at CIC bioGUNE (Spain). TgVole (1x)[101] mice inoculated in this study were obtained from the breeding colonies at CIC bioGUNE (Spain) and were inoculated at Neiker—Basque Institute for Agricultural Research and Development. This experiment adhered to the guidelines included in the Spanish law “Real Decreto 1201/2005 de 10 de Octubre” on protection of animals used for experimentation and other scientific purposes, which is based on the European Directive 86/609/EEC on Laboratory Animal Protection. The project was approved by the Ethical Committees on Animal Welfare (project code assigned by the Ethical Committee P-CBG-CBBA-0314) and performed under their supervision. The experiments involving Tg338 mice[102], obtained from a breeding colony from at the Autonomous University of Barcelona and inoculated at the IRTA-CReSA, were approved by

the animal experimentation ethics committee of the Autonomous University of Barcelona (Reference numbers: 5767 and 1124M2R) in agreement with Article 28, sections a), b), c) and d) of the "Real Decreto 214/1997 de 30 de Julio" and the European Directive 86/609/CEE and the European Council Guidelines included in the European Convention for the Protection of Vertebrate Animals used for Experimental and Other Scientific Purposes.

### *Bioassays/In vivo infectivity*

Spontaneously PMSA-generated rec-PrPres containing sample was diluted 1:10 in sterile PBS prior to intracerebral inoculation into TgVole (1x), and Tg338 mice. For the second passage, 10 % brain homogenates from mice inoculated with the recombinant ovine prion strain was prepared as 1 % (w/v) brain homogenates in PBS from an animal selected from the first passage showing an incubation period as close as possible to the group mean.

Groups of 5 to 6-week-old TgVole (1x) and Tg338 mice were inoculated intracerebrally with 20 µl of inocula into the left cerebral hemisphere using a sterile disposable 27-gauge hypodermic needle (Terumo). Mice were anesthetized with gaseous anesthesia (Isoflurane, IsoVet®, Braun). Experimental groups were comprised of 6 to 12 animals each as indicated in the corresponding table. The animals were examined twice a week until development of neurological clinical signs, after which they were examined daily. Clinically affected animals were culled at an advanced stage of disease, but before neurological impairment compromised their welfare, by exposure to a rising concentration of carbon dioxide. The clinical signs monitored included kyphosis, gait abnormalities, altered coat state, depressed mental state, flattened back, eye discharge, hyperactivity, loss of body condition, and incontinence. Animals exhibiting two or more severe signs or invalidating motor disturbances were euthanized. Survival time was calculated as the interval between inoculation and culling or death. The brain was extracted immediately after culling and divided longitudinally; one half of the brain was kept frozen at -80 °C for biochemical analysis and the other part was placed into 10 % phosphate-buffered formalin solution (Sigma-Aldrich) for histopathological analysis.

### *Production and labeling of synthetic recombinant ovine prions*

Ovine prions (ovPrPSc) are a courtesy of Prof. Joaquin Castilla and were produced by misfolding of the monomeric ovine prion protein (VRQ) as follows: as reported previously for hundreds of distinct rec-PrP variants[40], the PMSA substrate containing ovine VRQ rec-PrP and dextran sulfate was complemented with 0.1 and 1 mm-diameter acid-washed glass beads (BioSpec Products, Inc.), and up to 8 independent PMSA reactions were set, at 39 °C and with continuous shaking at 700 rpm using a Digital shaking Drybath (Thermo Scientific) for 24 h. Four serial 24h-PMSA rounds were done for each reaction, diluting 1:10 the product from the previous round into fresh substrate complemented with the same type of beads. Once misfolded, proteinase K-resistant rec-PrP (PrPres) was detected in any of the 8 replicates, this PMSA product was used as propagation seed to stabilize the strain, performing three serial PMSA rounds. Briefly the original PMSA product was diluted 1:100 in fresh

substrate, complemented in this case with 1 mm-diameter zirconia-silicate beads (BioSpec Products, Inc.), that promote prion propagation but not spontaneous misfolding. After 3 serial 24h PMSA rounds at 1:100 dilution, the recombinant prions were loaded into clean zirconia silicate beads for long term storage and subsequent propagation or expansions, as detailed in[62]. These prion-loaded beads were used as seeds to prepare large volume batches of recombinant ovine prions (ovPrPSc) used for labeling and internalization studies.

Prions were labelled with AlexaFluor488-NHS ester (Invitrogen, A20000) following manufacturer's instructions. Prions were centrifuged at 18000 g at 4°C for 20 minutes to pellet aggregates. Supernatant was removed, prions were resuspended in PBS + 0.1% sarkosyl (w/v) and sonicated in a high-power water bath sonicator (Telsonic Ultrasonics) for 10 minutes (30s ON – 30s OFF cycles) at approximately 150 W and 40 kHz. For quantification, 7 mL of prion suspension were diluted in 63 uL of ultrapure GdnHCl 8M, incubated for 5 minutes at room temperature to dissociate the fibrils and then absorbance was measured at 280 nm using a benchtop spectrophotometer. To calculate the monomer equivalent concentration of each prion preparation, we used the following parameters: MW:22057.3 Da, molar extinction coefficient: 52495. Prions were resuspended at the final concentration of 1 mg/mL and incubated with AlexaFluor488 NHS ester in a 1: 12.5 ratio for 1 hour at room temperature on a rotating wheel, protected from light. Excess unreacted dye was removed with 4 rounds of centrifugation and resuspension in PBS + 0.1% sarkosyl. Finally, prions were resuspended at the final concentration of 0.4 mg/mL (18 mM), aliquoted and stored at -20°C.

### *Flow cytometry*

All experiments to establish the assay for prion uptake and the genome-wide primary screen were acquired on the BD FACS Aria III (BD Biosciences). Arrayed secondary screens on endocytosis and internalization of a-synuclein pre-formed fibrils were acquired on the LSRFortessa Flow Cytometer (BD Biosciences) using the High Throughput Sampler (HTS) in Standard mode. Pooled secondary screen for validation of prion uptake modifiers was acquired on the Sony SH800 sorter (Sony Biotechnology Inc). Validation experiments of individual hits were acquired on the Sony SP6800 Flow Cytometer (Sony Biotechnology Inc).

For prion uptake experiments, 100'000 cells/well were plated in 24-well plates. The day after, culture medium was removed and replaced with 1 mL/well of OptiMEM + 10% FBS containing ovPrPSc-488 prions at 100 nM final concentration. After 24 hours of incubation, cells were washed two times with PBS, trypsinized to remove unbound prions and washed again two times in PBS before being resuspended in FACS buffer (PBS, 2% BSA, 0.5 mM EDTA, 1% Accutase) and analyzed. When checking internalization with Trypan Blue, samples were first acquired at the cytometer, then Trypan Blue was added at the final concentration of 2 mM (1:2 dilution of the commercial Trypan Blue solution, Gibco, 15250061) and samples were reacquired with the same acquisition settings. Cell viability was measured by adding the live/dead stain Zombie NIR

### *Whole-genome screen*

The human T.gonfio CRISPR activation library was packaged into lentiviruses in arrayed format following the protocol described in 33. Individual lentiviruses were pooled together, and the resulting mix was titrated as described above. The library was transduced into SH-KOvp64 at a multiplicity of infection (MOI) of 0.3 at an estimated coverage of 500 cells expressing each set of 4sg guides, using transduction conditions described above. 24 hours after infection, cells were placed under selection with puromycin at 2 ug/mL final concentration to remove uninfected cells. Cells were allowed to grow for 7 days under constant puromycin selection. At 8 days from the initial seeding, cells were reseeded into culture vessels at a density of 1 cell in 0.019 mm2. The day after, medium was replaced with antibiotic-free OptiMEM supplemented with 10% FBS and ovPrPSc-488 at 100 nM final concentration. After 24 hours of incubation, cells were prepared for FACS sorting on the BD FACS Aria III as described above. Cells were gated using forwards and side scatter to exclude dead cells, debris and unbound prions, then gated on the area vs. height of forward scatter to isolate single cells. Singlets were then gated on the BFP signal (sgRNA library) and on AlexaFluor 488 signal (ovPrPSc) using sgRNA-uninfected cells and prion-untreated cells to establish thresholds. 35% top ("prion positives") and 35% bottom ("prion negatives") populations were sorted using a custom-made purity mask. Purity of the sorted populations was confirmed by subsequent reanalysis. Sorted cells were pelleted and stored at -80°C.

### *Genomic DNA extraction*

Cell pellets collected during primary screen were incubated overnight in Tris-EDTA pH 8 supplemented with SDS (2% final concentration) and proteinase K (2 mg/mL final concentration) at 50°C and 500 rpm constant shaking. The next days, samples were transferred to new tubes, two volumes of chaos buffer (ex: for 10*106 cells, 2.5 mL of lysis buffer and 5 mL of chaos buffer were used) were added, and samples were incubated at 37°C under slow constant stirring for at least 2 hours. These two steps ensure a thorough cell lysis and the removal of prion infectivity. Next, samples were subjected to three subsequent rounds of extraction using phenol:chloroform:isoamyl alcohol (25:24:1) consisting of 30 min incubation with 1.5 volumes of Ph:Chl:IAA and 30 min of centrifugation at 5000 g to separate phases. After each centrifugation, the aqueous phase containing gDNA was transferred to clean tubes, paying attention to not disturb the interphase. To remove residual phenol, a fourth extraction step consisting of a 30 min incubation step with chloroform followed by centrifugation for 10 min at 5000 g was performed. The recovered phase was then mixed with cold ethanol (2 volumes), 4% (v/v) sodium acetate (Sigma) and GlycoBlue (Invitrogen), and incubated overnight at -20°C. Next, gDNA was precipitated by centrifugation at 5000 g for 30 min. gDNA pellets were washed three times in excess 70% ethanol (15 min incubation followed by centrifugation for 10 min at 10'000g), then left to dry to remove residual ethanol and resuspended in 10 mM Tris-HCl pH 8. To ensure proper resuspension, samples were incubated in buffer overnight at 37°C before being

collected. gDNA quantification was performed using Qubit (ThermoFisher Scientific, 1X dsDNA Broad Range Quantification Kit, Q32853).

### *sgRNA guides and NGS sequencing*

sgRNAs were amplified by PCR reactions as previously described 33. The following barcoded forward primers were used:

| Forward primer | Sequence | Barcode |
|---|---|---|
| FW_A | ATGATACGGCGACCACCGAGATCTACACCAGTGCTTTTTGAGACTATAAATATCCCTTGGAGAAAAGCCTTGTTTG | CAGTGCTT |
| FW_B | AATGATACGGCGACCACCGAGATCTACACTCCATTACTTTGAGACTATAAATATCCCTTGGAGAAAAGCCTTGTTTG | TCCATTAC |
| FW_C | AATGATACGGCGACCACCGAGATCTACACGTCGACTGTTTGAGACTATAAATATCCCTTGGAGAAAAGCCTTGTTTG | GTCGACTG |
| FW_D | AATGATACGGCGACCACCGAGATCTACACAGTACGCCTTTGAGACTATAAATATCCCTTGGAGAAAAGCCTTGTTTG | AGTACGCC |
| FW_E | AATGATACGGCGACCACCGAGATCTACACTAGGCAGTTTTGAGACTATAAATATCCCTTGGAGAAAAGCCTTGTTTG | TAGGCAGT |
| FW_F | AATGATACGGCGACCACCGAGATCTACACCTAATGGATTTGAGACTATAAATATCCCTTGGAGAAAAGCCTTGTTTG | CTAATGGA |
| FW_G | AATGATACGGCGACCACCGAGATCTACACCCTGCATATTTGAGACTATAAATATCCCTTGGAGAAAAGCCTTGTTTG | CCTGCATA |
| FW_H | AATGATACGGCGACCACCGAGATCTACACGTATCTCATTTGAGACTATAAATATCCCTTGGAGAAAAGCCTTGTTTG | GTATCTCA |

Clean-up of PCR products from reaction components and primer dimers was performed using SPRIselect Beads (Beckman Coulter, B23317) following manufacturer's instructions. Samples were pooled together and sequenced on an Illumina NextSeq 2000 instrument using a P2 flowcells and a 300 cycles Illumina Cartridge.

### *CRISPR screens data analysis*

Data analysis was performed using the Sushi platform[103] (FGCZ, University of Zurich) and R (version 4.5.1). Reads quality was assessed using FastQC tool (version 0.12.0)[104]. One sample from the secondary screen with abnormally high GC% (>70%) content was excluded from further analysis. By mapping sgRNA-2 and sgRNA-3 sequences to the Human T.Gonfio CRISPR activation library, we quantified their absolute abundance in each condition and identified the associated target gene. Reads were normalized across conditions using the median ratios method implemented by the R package DESeq2 (version 3.22)[105]. Differential guide enrichment was performed using DESeq2[106]. Candidate hits were defined according to the following criteria: p-value (unadjusted) ≤ 0.05, and $\log_2$ Fold change ≤ -0.3 or ≥ 0.3 for downregulators and upregulators, respectively. Correlation between replicates was expressed as Pearson's correlation coefficient. Over Representation Analysis (ORA) on candidate hits was performed using the R package ClusterProfiler (version 3.2)[107].

The genomic localization of hits was visualized with a custom script developed by A.A. (https://github.com/aagaag/ManhattanCrispr).

### *Secondary screen*

Selected candidate genes were manually picked from the T.gonfio arrayed library in the form of glycostocks, amplified as described in 33 and distributed in four 96 deep-well plates. Plasmid extraction was carried out as follows: 50 μL of bacterial cultures were transferred in new 96 deep-well plates containing 1.2 mL of Terrific Broth with 15 µg/ml trimethoprim (Sigma, cat. #T7883-5G) and 15 µg/ml tetracycline (Sigma, cat. #T3258-5G) using ViaFlo (Integra). Plates were grown for 48 h at 30°C and 1100 rpm shaking on a thermal shaker (http://www.rooyn.com/products/446/2459.aspx, cat.# RS300). Bacteria were pelleted by centrifugation at 4000 rpm for 20 min and pellets were resuspended in 200 μL P1 buffer followed by 200 μL of lysis buffer P2 and 200 μL of neutralizing buffer P3. After each step, samples were mixed using ViaFlo to ensure proper reagent mixing. Plates were then centrifuged at maximum speed for 10 minutes to pellet chromosomal DNA and bacterial debris. Supernatants were transferred to new 96 deep-well plates and 2 volumes of cold ethanol were added. Plasmidic DNA was precipitated by centrifugation at maximum speed for 10 min, then pellets were air-dried and resuspended in 50 μL of ddH2O by vortexing. DNA was bound to Sera Mag Select Beads by incubation at room temperature for 10 minutes and washed for two times with 1 mL of 70% ethanol. Beads were then air-dried and bound DNA was eluted in 125 μL of Tris-EDTA pH 8. To ensure proper elution, plates were incubated at 65°C for 10 minutes before transferring the eluted DNA to new plates. 10 randomly selected wells per plate were quantified using Nanodrop. The resulting averaged concentration was applied to the entire plate.

Individual plasmids were packaged into lentiviruses in arrayed format as done for the genome-wide library 33. A portion of the lentiviral-containing supernatants (30 mL/lentivirus) were pooled to generate the secondary screen pooled library, while the remaining volume was aliquoted into arrayed 384-well plates and stored at -80°C.

Pooled secondary screen was carried out following the same protocol of the genome-wide primary screen, except for the starting coverage that was expanded to 5000X. Differently from the genome-wide screen, FACS sorting of the secondary screen samples was carried out on a Sony SH800 sorter (Sony Biotechnology Inc.). The screen was performed in three independent replicates and samples were sequenced all together on an Illumina NextSeq 2000 instrument (Illumina).

### *Cytotoxicity assay*

Cells were seeded in 96-well plates with opaque wells at the final density of 4500 cells/well. The day after, cells were treated with increasing concentrations of unlabelled or fluorescent ovPrP$^{Sc}$ for 24 hours. Viability was measured using CellTiter-Glo 2.0 (Promega) and read on the Envision plate reader (Revvity).

### *Purification of recombinant neurodegeneration-related proteins (TauK18, α-synuclein, Amyloidβ 1-42) and preparation of pre-formed fibrils*

Monomeric TauK18 fragment was purified as described in [55]. Aggregation was carried out in a FLUOstar Omega (BMG Labtech) plate reader following the protocol described in [55]. Monomeric α-synuclein was purified as described in [108]. Aggregation was carried out in a benchtop thermoblock following the protocol described in [109]. Aβ1-42 peptide was purified as described in [110]. Aggregation was carried out in a benchtop thermoblock following the protocol described in [110].

### *Arrayed secondary screens for endocytosis modifiers*

SH-KO$^{vp64}$ cells were seeded in 96-well plate at a density of 10'000 cells/well. The day after, cells were transduced with arrayed lentiviruses at an MOI of 3. Transduction was carried out in OPTIMeM + 10% FBS + Polybrene 8 ug/mL, and a reduced volume of 40 uL/well was used. One day after transduction, virus-containing medium was replaced with fully supplemented OPTIMeM. Cells were cultured for 5 days after transduction and then treated with either endocytic probes or amyloid aggregates. Treatments were performed as follows:

| Treatment | Final concentration | Incubation time (h) |
|---|---|---|
| Tau K18 PFFs-488 | 100 nM | 24 |
| a-synuclein PFFs-647 | 100 nM | 24 |
| Amyloid b-647 | 100 nM | 24 |
| Dextran-Fluorescein 70 kDa | 125 mg/mL | 24 |
| Transferrin-647 | 500 nM | 0.5 |
| E.coli pHRodo Green Bioparticles | 100 mg/mL | 2 |

The day of the analysis, cells were washed 2 times with PBS, then detached with Trypsin and neutralized with FACS buffer containing 2% FBS/PBS. After thorough in-well mixing, cells were analyzed using a LSRFortessa Flow Cytometer (BD Biosciences) equipped with a High Throughput Sampler.

To check for effects of hit genes on cell growth, cells were seeded on poly-D-lysine coated 96-well plates (Greiner) and grown for 5 days after transduction. Cells were then fixed with 4% PFA/PBS for 15 minutes and incubated with Hoechst dye (1:10'000) for 15 minutes for nuclei staining. Imaging was carried out on a GE InCell Analyzer 2500HS widefield microscope (Cytiva life sciences).

### *Immunoblotting*

Cell lysates were prepared in lysis buffer (50 mM Tris–HCl, pH 8, 150 mM NaCl, 0.5% sodium deoxycholate, and 0.5% Triton-X 100) supplemented with protease inhibitors (cOmplete Protease Inhibitor Cocktail, Sigma-Aldrich). The bicinchoninic acid assay (BCA) was used to measure the total protein concentrations according to the manufacturer's instructions (Pierce). Samples were boiled at 95 °C in NuPAGE LDS Sample Buffer 1x (Invitrogen) supplemented with 1 mM DTT (Sigma-Aldrich), loaded onto precast gels (4-12% Bis-Tris NuPage gels, Invitrogen), and blotted onto PVDF membranes (Invitrogen).

The following antibodies were used: anti-Cas9 1:1000 (Cell Signaling, #14697), anti-actin HRP conjugated 1:10'000 (Sigma-Aldrich, A3854), anti-Rab13 1:1000 (Abcam, ab180936), anti-ADAM10 1:1000 (Abcam, ab124695), anti-vinculin 1:1000 (Abcam, ab129002), anti-PrP POM2 0.3 mg/mL, anti-PrP POM1 0.3 mg/mL, anti phospho SMAD1/5 (CellSignaling #9516), anti pERK1/2 (CellSignaling #4370), anti phospho AKT (CellSignaling #4060), anti phospho p38 MAPK (CellSignaling #9211), anti-total p38 MAPK (CellSignaling #9212), anti-Rabbit-HRP 1:10'000 (Jackson ImmunoResearch #111-035-045), anti-Mouse-HRP 1:10'000 (Jackson ImmunoResearch #115-035-005), anti-Goat-HRP 1:10'000 (Jackson ImmunoResearch #705-035-147).

### *Transcriptomics*

Transcriptomic analysis was performed on six different human cell lines (HovH, HovS, HovL), each infected with either non-infectious (NBH) or prion-infected (PG127) brain homogenates. Each line was tested in four biological replicates, corresponding to individual frozen aliquots. Cell pellets were collected and total RNA was extracted using the RNeasy Mini kit (Qiagen) following manufacturer's instructions. RNA integrity was measured using the Agilent 4200 Tapestation system (Agilent) and all samples exhibited RNA Integrity Number (RIN) higher than 9. mRNAs were enriched using poly-dT-beads, then fragmented, ligated to sequencing adaptors and retro-transcribed into cDNA. Libraries were amplified by PCR and sequenced using a NovaSeq X Plus platform (Illumina) with paired-end 150 bp reads. Sequencing was performed in a multiplexed run with a total read depth of approximately 500 million reads, corresponding to ~21 million reads per sample.

Sequencing data were analyzed using the Sushi platform[103] (FGCZ, University of Zurich) and R (version 4.5.1). Reads quality was assessed using FastQC tool (version 0.12.0)[104] , transcript alignment was perfomed using STAR package (version 2.7.11b)[111] (ref) and raw counts were normalized using TPM (transcript per kilobase million). Differential gene expression analysis was conducted using R package DESeq2 (version 3.22)[106]. Upregulated transcripts were identified by $\log_2$ Fold change ≥ 1 and adjusted (Benjamini-Hochberg) p-value < 0.05, while downregulated transcripts were identified by $\log_2$ Fold change ≤ -1 and adjusted (Benjamini-Hochberg) p-value < 0.05. Over Representation Analysis (ORA) on differentially expressed genes was performed using the R package ClusterProfiler (version 3.2)[107].

## References


1 Aguzzi, A. & De Cecco, E. Shifts and drifts in prion science. *Science* **370**, 32-34 (2020). https://doi.org/10.1126/science.abb8577

2 Fraser, H. Neuronal spread of scrapie agent and targeting of lesions within the retino-tectal pathway. *Nature* **295**, 149-150 (1982). https://doi.org/10.1038/295149a0

3 Kimberlin, R. H. & Walker, C. A. Pathogenesis of Scrapie (Strain 263K) in Hamsters Infected Intracerebrally, Intraperitoneally or Intraocularly. *Journal of General Virology* **67**, 255-263 (1986). https://doi.org/https://doi.org/10.1099/0022-1317-67-2-255

4 Caredio, D. *et al.* Gpnmb Defines a Phagocytic State of Microglia Linked to Neuronal Loss in Prion Disease. *bioRxiv*, 2025.2002.2011.637592 (2025). https://doi.org/10.1101/2025.02.11.637592

5 Liu, Y. *et al.* NG2 glia protect against prion neurotoxicity by inhibiting microglia-to-neuron prostaglandin E2 signaling. *Nature Neuroscience* **27**, 1534-1544 (2024). https://doi.org/10.1038/s41593-024-01663-x

6 Aguzzi, A. & Weissmann, C. A suspicious signature. *Nature* **383**, 666-667 (1996). https://doi.org/10.1038/383666a0

7 Goold, R. *et al.* Rapid cell-surface prion protein conversion revealed using a novel cell system. *Nature Communications* **2**, 281 (2011). https://doi.org/10.1038/ncomms1282

8 Priola, S. A. in *Handbook of Clinical Neurology* Vol. 153 (eds Maurizio Pocchiari & Jean Manson) 45-68 (Elsevier, 2018).

9 Borchelt, D. R., Taraboulos, A. & Prusiner, S. B. Evidence for synthesis of scrapie prion proteins in the endocytic pathway. *J Biol Chem* **267**, 16188-16199 (1992).

10 Yim, Y. I. *et al.* The multivesicular body is the major internal site of prion conversion. *J Cell Sci* **128**, 1434-1443 (2015). https://doi.org/10.1242/jcs.165472

11 McKinley, M. P. *et al.* Ultrastructural localization of scrapie prion proteins in cytoplasmic vesicles of infected cultured cells. *Lab Invest* **65**, 622-630 (1991).

12 Veith, N. M., Plattner, H., Stuermer, C. A. O., Schulz-Schaeffer, W. J. & Bürkle, A. Immunolocalisation of PrPSc in scrapie-infected N2a mouse neuroblastoma cells by light and electron microscopy. *European Journal of Cell Biology* **88**, 45-63 (2009). https://doi.org/https://doi.org/10.1016/j.ejcb.2008.08.001

13 Ribes, J. M. *et al.* Prion protein conversion at two distinct cellular sites precedes fibrillisation. *Nature Communications* **14**, 8354 (2023). https://doi.org/10.1038/s41467-023-43961-1

14 Ballmer, B. A. *et al.* Modifiers of prion protein biogenesis and recycling identified by a highly parallel endocytosis kinetics assay. *J Biol Chem* **292**, 8356-8368 (2017). https://doi.org/10.1074/jbc.M116.773283

15 Mabbott, N. A. How do PrP(Sc) Prions Spread between Host Species, and within Hosts? *Pathogens* **6** (2017). https://doi.org/10.3390/pathogens6040060

16 Kujala, P. *et al.* Prion Uptake in the Gut: Identification of the First Uptake and Replication Sites. *PLOS Pathogens* **7**, e1002449 (2011). https://doi.org/10.1371/journal.ppat.1002449

17 Urayama, A. *et al.* Prions efficiently cross the intestinal barrier after oral administration: Study of the bioavailability, and cellular and tissue distribution in vivo. *Scientific Reports* **6**, 32338 (2016). https://doi.org/10.1038/srep32338

18 Donaldson, D. S. *et al.* M cell-depletion blocks oral prion disease pathogenesis. *Mucosal Immunology* **5**, 216-225 (2012). https://doi.org/https://doi.org/10.1038/mi.2011.68

19 Heppner, F. L. *et al.* Transepithelial prion transport by M cells. *Nat Med* **7**, 976-977 (2001). https://doi.org/10.1038/nm0901-976

20 Marshall, A., Bradford, B. M., Clarke, A. R., Manson, J. C. & Mabbott, N. A. Oral Prion Neuroinvasion Occurs Independently of PrP(C) Expression in the Gut Epithelium. *J Virol* **92** (2018). https://doi.org/10.1128/jvi.01010-18

21 Fehlinger, A. *et al.* Prion strains depend on different endocytic routes for productive infection. *Sci Rep* **7**, 6923 (2017). https://doi.org/10.1038/s41598-017-07260-2

22 Kanu, N. *et al.* Transfer of Scrapie Prion Infectivity by Cell Contact in Culture. *Current Biology* **12**, 523-530 (2002). https://doi.org/10.1016/S0960-9822(02)00722-4

23 Victoria, G. S., Arkhipenko, A., Zhu, S., Syan, S. & Zurzolo, C. Astrocyte-to-neuron intercellular prion transfer is mediated by cell-cell contact. *Scientific Reports* **6**, 20762 (2016). https://doi.org/10.1038/srep20762

24 Gousset, K. *et al.* Prions hijack tunnelling nanotubes for intercellular spread. *Nature Cell Biology* **11**, 328-336 (2009). https://doi.org/10.1038/ncb1841

25 Cheng, L., Zhao, W. & Hill, A. F. Exosomes and their role in the intercellular trafficking of normal and disease associated prion proteins. *Molecular Aspects of Medicine* **60**, 62-68 (2018). https://doi.org/https://doi.org/10.1016/j.mam.2017.11.011

26 Thomzig, A., Schulz-Schaeffer, W., Kratzel, C., Mai, J. & Beekes, M. Preclinical deposition of pathological prion protein PrPSc in muscles of hamsters orally exposed to scrapie. *The Journal of Clinical Investigation* **113**, 1465-1472 (2004). https://doi.org/10.1172/JCI21083

27 Künzi, V. *et al.* Unhampered prion neuroinvasion despite impaired fast axonal transport in transgenic mice overexpressing four-repeat tau. *J Neurosci* **22**, 7471-7477 (2002). https://doi.org/10.1523/jneurosci.22-17-07471.2002

28 Shearin, H. & Bessen, R. A. Axonal and transynaptic spread of prions. *J Virol* **88**, 8640-8655 (2014). https://doi.org/10.1128/jvi.00378-14

29 Magalhães, A. C. *et al.* Uptake and Neuritic Transport of Scrapie Prion Protein Coincident with Infection of Neuronal Cells. *The Journal of Neuroscience* **25**, 5207-5216 (2005). https://doi.org/10.1523/jneurosci.0653-05.2005

30 Leucht, C. *et al.* The 37 kDa/67 kDa laminin receptor is required for PrP(Sc) propagation in scrapie-infected neuronal cells. *EMBO Rep* **4**, 290-295 (2003). https://doi.org/10.1038/sj.embor.embor768

31 Horonchik, L. *et al.* Heparan sulfate is a cellular receptor for purified infectious prions. *J Biol Chem* **280**, 17062-17067 (2005). https://doi.org/10.1074/jbc.M500122200

32 Jen, A. *et al.* Neuronal low-density lipoprotein receptor-related protein 1 binds and endocytoses prion fibrils via receptor cluster 4. *J Cell Sci* **123**, 246-255 (2010). https://doi.org/10.1242/jcs.058099

33 Yin, J.-A. *et al.* Arrayed CRISPR libraries for the genome-wide activation, deletion and silencing of human protein-coding genes. *Nature Biomedical Engineering* (2024). https://doi.org/10.1038/s41551-024-01278-4

34 Kampmann, M. A CRISPR Approach to Neurodegenerative Diseases. *Trends Mol Med* **23**, 483-485 (2017). https://doi.org/10.1016/j.molmed.2017.04.003

35 Tian, R. *et al.* CRISPR Interference-Based Platform for Multimodal Genetic Screens in Human iPSC-Derived Neurons. *Neuron* **104**, 239-255.e212 (2019). https://doi.org/10.1016/j.neuron.2019.07.014

36 Pease, D. *et al.* Genome-wide identification of microRNAs regulating the human prion protein. *Brain Pathol* **29**, 232-244 (2019). https://doi.org/10.1111/bpa.12679

37 Jinek, M. *et al.* A programmable dual-RNA-guided DNA endonuclease in adaptive bacterial immunity. *Science* **337**, 816-821 (2012). https://doi.org/10.1126/science.1225829

38 Hazards, E. P. o. B. Scientific Opinion on a request for a review of a scientific publication concerning the zoonotic potential of ovine scrapie prions. *EFSA Journal* **13**, 4197 (2015). https://doi.org/https://doi.org/10.2903/j.efsa.2015.4197

39 Gombojav, A. *et al.* Susceptibility of Transgenic Mice Expressing Chimeric Sheep, Bovine and Human PrP Genes to Sheep Scrapie. *Journal of Veterinary Medical Science* **65**, 341-347 (2003). https://doi.org/10.1292/jvms.65.341

40 Eraña, H. *et al.* A Protein Misfolding Shaking Amplification-based method for the spontaneous generation of hundreds of bona fide prions. *Nat Commun* **15**, 2112 (2024). https://doi.org/10.1038/s41467-024-46360-2

41 Marcon, A. *et al.* Transplantation Blues: Inadvertent Staining of Amyloid Deposits With Trypan Blue. *Cornea* **37**, 824-828 (2018). https://doi.org/10.1097/ico.0000000000001591

42 Karpowicz, R. J., Jr. *et al.* Selective imaging of internalized proteopathic α-synuclein seeds in primary neurons reveals mechanistic insight into transmission of synucleinopathies. *J Biol Chem* **292**, 13482-13497 (2017). https://doi.org/10.1074/jbc.M117.780296

43 Burstyn-Cohen, T. & Fresia, R. TAM receptors in phagocytosis: Beyond the mere internalization of particles. *Immunological Reviews* **319**, 7-26 (2023). https://doi.org/https://doi.org/10.1111/imr.13267

44 Rotshenker, S. *et al.* Galectin-3/MAC-2, Ras and PI3K activate complement receptor-3 and scavenger receptor-AI/II mediated myelin phagocytosis in microglia. *Glia* **56**, 1607-1613 (2008). https://doi.org/10.1002/glia.20713

45 Björkblom, B. *et al.* c-Jun N-terminal kinase phosphorylation of MARCKSL1 determines actin stability and migration in neurons and in cancer cells. *Mol Cell Biol* **32**, 3513-3526 (2012). https://doi.org/10.1128/mcb.00713-12

46 Avar, M. *et al.* Prion infection, transmission, and cytopathology modeled in a low-biohazard human cell line. *Life Science Alliance* **3**, e202000814 (2020). https://doi.org/10.26508/lsa.202000814

47 Sellitto, S. *et al.* Prion propagation is controlled by a hierarchical network involving the nuclear Tfap2c and hnRNP K factors and the cytosolic mTORC1 complex. *bioRxiv*, 2024.2010.2021.619371 (2025). https://doi.org/10.1101/2024.10.21.619371

48 Oren, T., Torregroza, I. & Evans, T. An Oct-1 binding site mediates activation of the gata2 promoter by BMP signaling. *Nucleic Acids Res* **33**, 4357-4367 (2005). https://doi.org/10.1093/nar/gki746

49 Dalgin, G. *et al.* GATA-2 functions downstream of BMPs and CaM KIV in ectodermal cells during primitive hematopoiesis. *Dev Biol* **310**, 454-469 (2007). https://doi.org/10.1016/j.ydbio.2007.08.012

50 Dobrzycki, T., Lalwani, M., Telfer, C., Monteiro, R. & Patient, R. The roles and controls of GATA factors in blood and cardiac development. *IUBMB Life* **72**, 39-44 (2020). https://doi.org/https://doi.org/10.1002/iub.2178

51 Brown, A. C. *et al.* Role for compartmentalization in nephron progenitor differentiation. *Proceedings of the National Academy of Sciences* **110**, 4640-4645 (2013). https://doi.org/doi:10.1073/pnas.1213971110

52 Tsujimura, T., Idei, M., Yoshikawa, M., Takase, O. & Hishikawa, K. Roles and regulation of bone morphogenetic protein-7 in kidney development and diseases. *World J Stem Cells* **8**, 288-296 (2016). https://doi.org/10.4252/wjsc.v8.i9.288

53 Oxburgh, L., Brown, A. C., Muthukrishnan, S. D. & Fetting, J. L. Bone morphogenetic protein signaling in nephron progenitor cells. *Pediatr Nephrol* **29**, 531-536 (2014). https://doi.org/10.1007/s00467-013-2589-2

54 Evans, L. D. *et al.* Tau uptake by human neurons depends on receptor LRP1 and kinase LRRK2. *The EMBO Journal* **44**, 5149-5186-5186 (2025). https://doi.org/https://doi.org/10.1038/s44318-025-00514-0

55 De Cecco, E. *et al.* The uptake of tau amyloid fibrils is facilitated by the cellular prion protein and hampers prion propagation in cultured cells. *J Neurochem* **155**, 577-591 (2020). https://doi.org/10.1111/jnc.15040

56 Holmes, B. B. *et al.* Heparan sulfate proteoglycans mediate internalization and propagation of specific proteopathic seeds. *Proceedings of the National Academy of Sciences* **110**, E3138-E3147 (2013). https://doi.org/doi:10.1073/pnas.1301440110

57 Wu, K.-M. *et al.* Neuronal FAM171A2 mediates α-synuclein fibril uptake and drives Parkinson's disease. *Science* **387**, 892-900 (2025). https://doi.org/doi:10.1126/science.adp3645

58 Chen, K. *et al.* LRP1 is a neuronal receptor for α-synuclein uptake and spread. *Molecular Neurodegeneration* **17**, 57 (2022). https://doi.org/10.1186/s13024-022-00560-w

59 Vanderperre, B. *et al.* A genome-wide CRISPR/Cas9 screen identifies genes that regulate the cellular uptake of α-synuclein fibrils by modulating heparan sulfate proteoglycans. *bioRxiv*, 2023.2009.2029.560170 (2024). https://doi.org/10.1101/2023.09.29.560170

60 Aulić, S. *et al.* α-Synuclein Amyloids Hijack Prion Protein to Gain Cell Entry, Facilitate Cell-to-Cell Spreading and Block Prion Replication. *Scientific Reports* **7**, 10050 (2017). https://doi.org/10.1038/s41598-017-10236-x

61 Emmenegger, M. *et al.* LAG3 is not expressed in human and murine neurons and does not modulate α-synucleinopathies. *EMBO Molecular Medicine* **13**, e14745 (2021). https://doi.org/https://doi.org/10.15252/emmm.202114745

62 Eraña, H. *et al.* Understanding the key features of the spontaneous formation of bona fide prions through a novel methodology that enables their swift and consistent generation. *Acta Neuropathol Commun* **11**, 145 (2023). https://doi.org/10.1186/s40478-023-01640-8

63 Greil, C. S. *et al.* Acute cellular uptake of abnormal prion protein is cell type and scrapie-strain independent. *Virology* **379**, 284-293 (2008). https://doi.org/https://doi.org/10.1016/j.virol.2008.07.006

64 Legname, G. & Scialò, C. On the role of the cellular prion protein in the uptake and signaling of pathological aggregates in neurodegenerative diseases. *Prion* **14**, 257-270 (2020). https://doi.org/10.1080/19336896.2020.1854034

65 Smith, L. M., Kostylev, M. A., Lee, S. & Strittmatter, S. M. Systematic and standardized comparison of reported amyloid-β receptors for sufficiency, affinity, and Alzheimer's disease relevance. *J Biol Chem* **294**, 6042-6053 (2019). https://doi.org/10.1074/jbc.RA118.006252

66 Corbett, G. T. *et al.* PrP is a central player in toxicity mediated by soluble aggregates of neurodegeneration-causing proteins. *Acta Neuropathol* **139**, 503-526 (2020). https://doi.org/10.1007/s00401-019-02114-9

67 Urrea, L., Ferrer, I., Gavín, R. & Del Río, J. A. The cellular prion protein (PrP(C)) as neuronal receptor for α-synuclein. *Prion* **11**, 226-233 (2017). https://doi.org/10.1080/19336896.2017.1334748

68 Lubeseder-Martellato, C. *et al.* Oncogenic KRas-induced Increase in Fluid-phase Endocytosis is Dependent on N-WASP and is Required for the Formation of Pancreatic

Preneoplastic Lesions. *EBioMedicine* **15**, 90-99 (2017). https://doi.org/10.1016/j.ebiom.2016.12.013

69 Zhou, L. & Matsushima, G. K. Tyro3, Axl, Mertk receptor-mediated efferocytosis and immune regulation in the tumor environment. *Int Rev Cell Mol Biol* **361**, 165-210 (2021). https://doi.org/10.1016/bs.ircmb.2021.02.002

70 Fourgeaud, L. *et al.* TAM receptors regulate multiple features of microglial physiology. *Nature* **532**, 240-244 (2016). https://doi.org/10.1038/nature17630

71 Lai, C. & Lemke, G. An extended family of protein-tyrosine kinase genes differentially expressed in the vertebrate nervous system. *Neuron* **6**, 691-704 (1991).

72 Prieto, A. L., O'Dell, S., Varnum, B. & Lai, C. Localization and signaling of the receptor protein tyrosine kinase Tyro3 in cortical and hippocampal neurons. *Neuroscience* **150**, 319-334 (2007).

73 Miao, S. *et al.* Tyro3 promotes the maturation of glutamatergic synapses. *Front Neurosci* **18**, 1327423 (2024). https://doi.org/10.3389/fnins.2024.1327423

74 Xiong, W. *et al.* Gas6 and the Tyro 3 receptor tyrosine kinase subfamily regulate the phagocytic function of Sertoli cells. *Reproduction* **135**, 77-87 (2008). https://doi.org/10.1530/rep-07-0287

75 Allen, L. & Aderem, A. A role for MARCKS, the alpha isozyme of protein kinase C and myosin I in zymosan phagocytosis by macrophages. *The Journal of experimental medicine* **182**, 829-840 (1995).

76 Mehrabian, M. *et al.* Prion Protein Deficiency Causes Diverse Proteome Shifts in Cell Models That Escape Detection in Brain Tissue. *PLoS One* **11**, e0156779 (2016). https://doi.org/10.1371/journal.pone.0156779

77 Walsh, A. B. & Bar-Sagi, D. Differential activation of the Rac pathway by Ha-Ras and K-Ras. *J Biol Chem* **276**, 15609-15615 (2001). https://doi.org/10.1074/jbc.M010573200

78 Yuan, F. *et al.* Macropinocytic dextran facilitates KRAS-targeted delivery while reducing drug-induced tumor immunity depletion in pancreatic cancer. *Theranostics* **12**, 1061-1073 (2022). https://doi.org/10.7150/thno.65299

79 Klumpe, H. E. *et al.* The context-dependent, combinatorial logic of BMP signaling. *Cell Systems* **13**, 388-407.e310 (2022). https://doi.org/10.1016/j.cels.2022.03.002

80 Huang, H. *et al.* BMP signaling pathway is required for commitment of C3H10T1/2 pluripotent stem cells to the adipocyte lineage. *Proc Natl Acad Sci U S A* **106**, 12670-12675 (2009). https://doi.org/10.1073/pnas.0906266106

81 Hemmati-Brivanlou, A. & Thomsen, G. H. Ventral mesodermal patterning in Xenopus embryos: Expression patterns and activities of BMP-2 and BMP-4. *Developmental Genetics* **17**, 78-89 (1995). https://doi.org/https://doi.org/10.1002/dvg.1020170109

82 Zou, H. & Niswander, L. Requirement for BMP Signaling in Interdigital Apoptosis and Scale Formation. *Science* **272**, 738-741 (1996). https://doi.org/doi:10.1126/science.272.5262.738

83 Kobayashi, T., Lyons, K. M., McMahon, A. P. & Kronenberg, H. M. BMP signaling stimulates cellular differentiation at multiple steps during cartilage development. *Proceedings of the National Academy of Sciences* **102**, 18023-18027 (2005). https://doi.org/doi:10.1073/pnas.0503617102

84 Wang, R. N. *et al.* Bone Morphogenetic Protein (BMP) signaling in development and human diseases. *Genes Dis* **1**, 87-105 (2014). https://doi.org/10.1016/j.gendis.2014.07.005

85 Nickel, J. & Mueller, T. D. Specification of BMP Signaling. *Cells* **8**, 1579 (2019).

86 Pinto, C., Cárdenas, P., Osses, N. & Henríquez, J. P. Characterization of Wnt/β-catenin and BMP/Smad signaling pathways in an in vitro model of amyotrophic lateral sclerosis. *Front Cell Neurosci* **7**, 239 (2013). https://doi.org/10.3389/fncel.2013.00239

87 Russo, K. & Wharton, K. A. BMP/TGF-β signaling as a modulator of neurodegeneration in ALS. *Dev Dyn* **251**, 10-25 (2022). https://doi.org/10.1002/dvdy.333

88 Affaneh, A. *et al.* Inhibition of Bone Morphogenetic Protein Signaling Prevents Tau Pathology in iPSC Derived Neurons and PS19 Mice. *Ann Neurol* **97**, 657-672 (2025). https://doi.org/10.1002/ana.27149

89 Zhang, X. *et al.* BMP4 overexpression induces the upregulation of APP/Tau and memory deficits in Alzheimer's disease. *Cell Death Discovery* **7**, 51 (2021). https://doi.org/10.1038/s41420-021-00435-x

90 Nakamura, Y., Ozaki, T., Koseki, H., Nakagawara, A. & Sakiyama, S. Accumulation of p27 KIP1 is associated with BMP2-induced growth arrest and neuronal differentiation of human neuroblastoma-derived cell lines. *Biochem Biophys Res Commun* **307**, 206-213 (2003). https://doi.org/10.1016/s0006-291x(03)01138-0

91 Hegarty, S. V., Sullivan, A. M. & O'Keeffe, G. W. BMP2 and GDF5 induce neuronal differentiation through a Smad dependant pathway in a model of human midbrain dopaminergic neurons. *Mol Cell Neurosci* **56**, 263-271 (2013). https://doi.org/10.1016/j.mcn.2013.06.006

92 Ferlemann, F. C., Menon, V., Condurat, A. L., Rößler, J. & Pruszak, J. Surface marker profiling of SH-SY5Y cells enables small molecule screens identifying BMP4 as a modulator of neuroblastoma differentiation. *Sci Rep* **7**, 13612 (2017). https://doi.org/10.1038/s41598-017-13497-8

93 Lauzon, M. A., Drevelle, O. & Faucheux, N. Peptides derived from the knuckle epitope of BMP-9 induce the cholinergic differentiation and inactivate GSk3beta in human SH-SY5Y neuroblastoma cells. *Sci Rep* **7**, 4695 (2017). https://doi.org/10.1038/s41598-017-04835-x

94 Jones, E. *et al.* Identification of novel risk loci and causal insights for sporadic Creutzfeldt-Jakob disease: a genome-wide association study. *Lancet Neurol* **19**, 840-848 (2020). https://doi.org/10.1016/s1474-4422(20)30273-8

95 Hong, N. *et al.* The transcription factor Sox7 modulates endocardiac cushion formation contributed to atrioventricular septal defect through Wnt4/Bmp2 signaling. *Cell Death Dis* **12**, 393 (2021). https://doi.org/10.1038/s41419-021-03658-z

96 Doyle, M. J. *et al.* Sox7 Regulates Lineage Decisions in Cardiovascular Progenitor Cells. *Stem Cells Dev* **28**, 1089-1103 (2019). https://doi.org/10.1089/scd.2019.0040

97 Ouzikov, S. *et al.* LRIG1 controls proliferation of adult neural stem cells by facilitating TGFβ and BMP signalling pathways. *Commun Biol* **7**, 845 (2024). https://doi.org/10.1038/s42003-024-06524-8

98 Chen, P. *et al.* MECOM promotes supporting cell proliferation and differentiation in cochlea. *J Otol* **17**, 59-66 (2022). https://doi.org/10.1016/j.joto.2021.11.002

99 Dumoulin, A., Zuñiga, N. R. & Stoeckli, E. T. Axon guidance at the spinal cord midline-A live imaging perspective. *J Comp Neurol* **529**, 2517-2538 (2021). https://doi.org/10.1002/cne.25107

100 Pérez-Castro, M. *et al.* Cofactors facilitate bona fide prion misfolding in vitro but are not necessary for the infectivity of recombinant murine prions. *PLoS Pathog* **21**, e1012890 (2025). https://doi.org/10.1371/journal.ppat.1012890

101 Fernández-Borges, N. *et al.* Cofactors influence the biological properties of infectious recombinant prions. *Acta Neuropathol* **135**, 179-199 (2018). https://doi.org/10.1007/s00401-017-1782-y

102 Vilotte, J. L. *et al.* Markedly increased susceptibility to natural sheep scrapie of transgenic mice expressing ovine prp. *J Virol* **75**, 5977-5984 (2001). https://doi.org/10.1128/jvi.75.13.5977-5984.2001

103 Hatakeyama, M. *et al.* SUSHI: an exquisite recipe for fully documented, reproducible and reusable NGS data analysis. *BMC Bioinformatics* **17**, 228 (2016). https://doi.org/10.1186/s12859-016-1104-8

104 Wingett, S. W. & Andrews, S. FastQ Screen: A tool for multi-genome mapping and quality control. *F1000Res* **7**, 1338 (2018). https://doi.org/10.12688/f1000research.15931.2

105 Love, M. I., Huber, W. & Anders, S. Moderated estimation of fold change and dispersion for RNA-seq data with DESeq2. *Genome Biology* **15**, 550 (2014). https://doi.org/10.1186/s13059-014-0550-8

106 Anders, S. & Huber, W. Differential expression analysis for sequence count data. *Genome Biol* **11**, R106 (2010). https://doi.org/10.1186/gb-2010-11-10-r106

107 Yu, G., Wang, L.-G., Han, Y. & He, Q.-Y. clusterProfiler: an R Package for Comparing Biological Themes Among Gene Clusters. *OMICS: A Journal of Integrative Biology* **16**, 284-287 (2012). https://doi.org/10.1089/omi.2011.0118

108 Neupane, S. *et al.* Large-scale bidirectional arrayed genetic screens identify <em>OXR1</em> and <em>EMC4</em> as modifiers of α-synuclein aggregation. *bioRxiv*, 2025.2006.2010.658866 (2025). https://doi.org/10.1101/2025.06.10.658866

109 Polinski, N. K. *et al.* Best Practices for Generating and Using Alpha-Synuclein Pre-Formed Fibrils to Model Parkinson's Disease in Rodents. *J Parkinsons Dis* **8**, 303-322 (2018). https://doi.org/10.3233/jpd-171248

110 Stine, W. B., Jungbauer, L., Yu, C. & LaDu, M. J. Preparing synthetic Aβ in different aggregation states. *Methods Mol Biol* **670**, 13-32 (2011). https://doi.org/10.1007/978-1-60761-744-0_2

111 Dobin, A. *et al.* STAR: ultrafast universal RNA-seq aligner. *Bioinformatics* **29**, 15-21 (2012). https://doi.org/10.1093/bioinformatics/bts635

112 Jones, E. *et al.* Identification of novel risk loci and causal insights for sporadic Creutzfeldt-Jakob disease: a genome-wide association study. *Lancet Neurol* **19**, 840-848 (2020). https://doi.org/10.1016/S1474-4422(20)30273-8

**Authors' contributions**

E.D.C.: designed, performed, contributed to, supervised and coordinated all experiments and analyses; execution of primary and secondary screens; data curation and visualization; manuscript writing. G.M.: performed bioinformatic analysis, data curation and visualization of primary and secondary screens and RNA-Seq results; contributed to all experiments shown in Fig. 1 to Fig. 5; assisted in experimental design and manuscript writing. C.M.: generated the HovH and HovL cell models; performed prion infection and maintenance of all prion-infected cell lines; performed RNA-Seq experiments (Fig. 4, Suppl. Fig. 8). D.C.: performed bioinformatic analysis, data curation and visualization of the primary screen (Fig. 2, Suppl. Fig. 4). H.E.: purified recombinant ovine PrP; produced synthetic ovPrP$^{Sc}$ aggregates and performed their biochemical characterization, including Transmission Electron Microscopy imaging (Fig. 1). C.A.: executed and assisted with validation experiments (Fig. 3-4). S.S.: data curation and visualization, manuscript writing. S.H.: assisted with the execution of the secondary screen (Fig. 2); purified Aβ peptide (Fig. 3); manuscript writing. C.S.: generated the farnesylated dTomato cell line used in Fig. 1F. J-A.Y.: designed and produced the T.gonfio CRISPR activation library. E.V.: inoculated mice with synthetic ovine prions and carried out all *in vivo* experiments to determine infectivity (Table 1). M.P.: manuscript writing and correction. J.C.: produced synthetic ovPrP$^{Sc}$ aggregates; data curation and visualization; manuscript writing. A.A.: project design and supervision; secured funding; generated the Manhattan plot in Suppl. Fig. 5; manuscript writing and correction.

**Funding and acknowledgements**

E.D.C. was recipient of the UZH postdoctoral grant (2020), the FreeNovation grant (2021-2022), the Synapsis Career Development Award (2022-2024, CDA-01), and is co-applicant with A.A. of the Parkinson Schweiz Grant (2023), the SNSF Projects and Applications Grant (2024) and the Uniscientia Grant (2025). J-AY. Was recipient of the UZH postdoctoral grant (2021) and of the Synapsis Career Development Award. S.H. was supported by the Michael J. Fox Foundation (MJFF-020710, MJFF-021073) and is supported by the Foundation for Research in Science and the Humanities at the University of Zurich (STWF-24-11) and the Innovation Fund of the University Hospital of Zurich (INOV00169). A.A. is supported by institutional core funding by the University of Zurich, a Distinguished Scientist Award of the NOMIS Foundation, and grants from the Michael J. Fox Foundation (grant ID MJFF-022156 and grant ID MJFF-024255), the Swiss National Science Foundation (SNSF grant ID 179040 and grant ID 207872, Sinergia grant ID 183563), the GELU Foundation, swissuniversities (CRISPR4ALL), the Human Frontiers Science Program (grant ID RGP0001/2022), the Parkinson Schweiz Foundation and the Uniscientia Foundation. We thank the following for their support: IKERBasque foundation, vivarium and maintenance from CIC bioGUNE and the personnel from (IRTA-CReSA), especially Dr. Enric Vidal and Samanta Giler, and the personnel from NEIKER for technical support. We thank Dr. Edoardo Marcora for his help on data analysis and Dr. Simon Mead

for sharing the list of sCJD-associated genomic loci[112]. We also thank Dr. Ilan Margalith, Joanna Zukowska and Sebastian Hachenberg for their help with lentivirus production, Evangelos Bouris. Andrea Armani and Geoffrey Howe for critical discussion, Dr. Susanne Kreutzer, Dr. Adriana Hotz and the Functional Genomics Center Zurich (FGCZ) for preparing sequencing libraries, CRISPR screen NGS sequencing, RNA Sequencing, quality control and technical support. The funders of the study had no role in study design, data collection, data analysis, data interpretation and manuscript writing. The corresponding authors had full access to all the data in the study and had final responsibility for the decision to submit for publication. Statistical analysis and graphs were generated with R (version 4.5.1) and GraphPad Prism version 10.2.0 for Windows and Mac, GraphPad Software, Boston, Massachussets USA, www.graphpad.com.

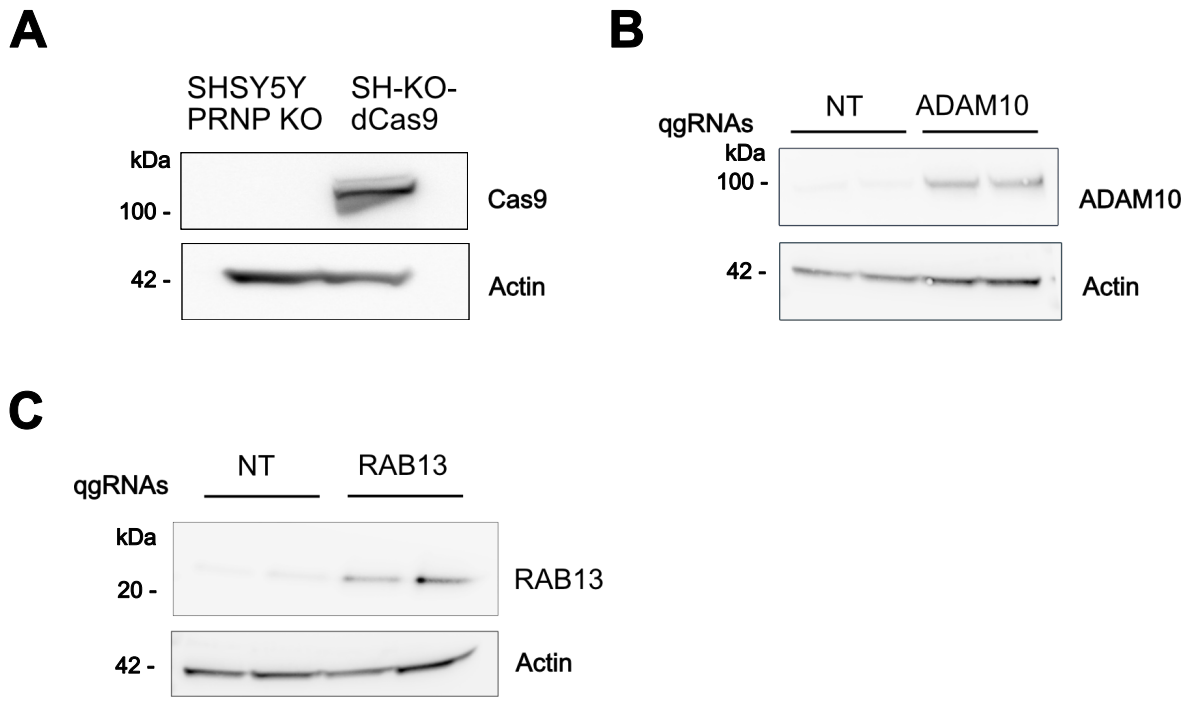


**Supplementary Figure 1. A.** Western Blot shows expression of the transactivator dCas9-VP64 in transduced cells compared to control cells. **B. and C.** Overexpression of randomly selected genes after 4 days from qgRNA lentiviral transduction confirms activity of the transactivator dCas9-VP64. Actin was used as loading control in all Western Blots.

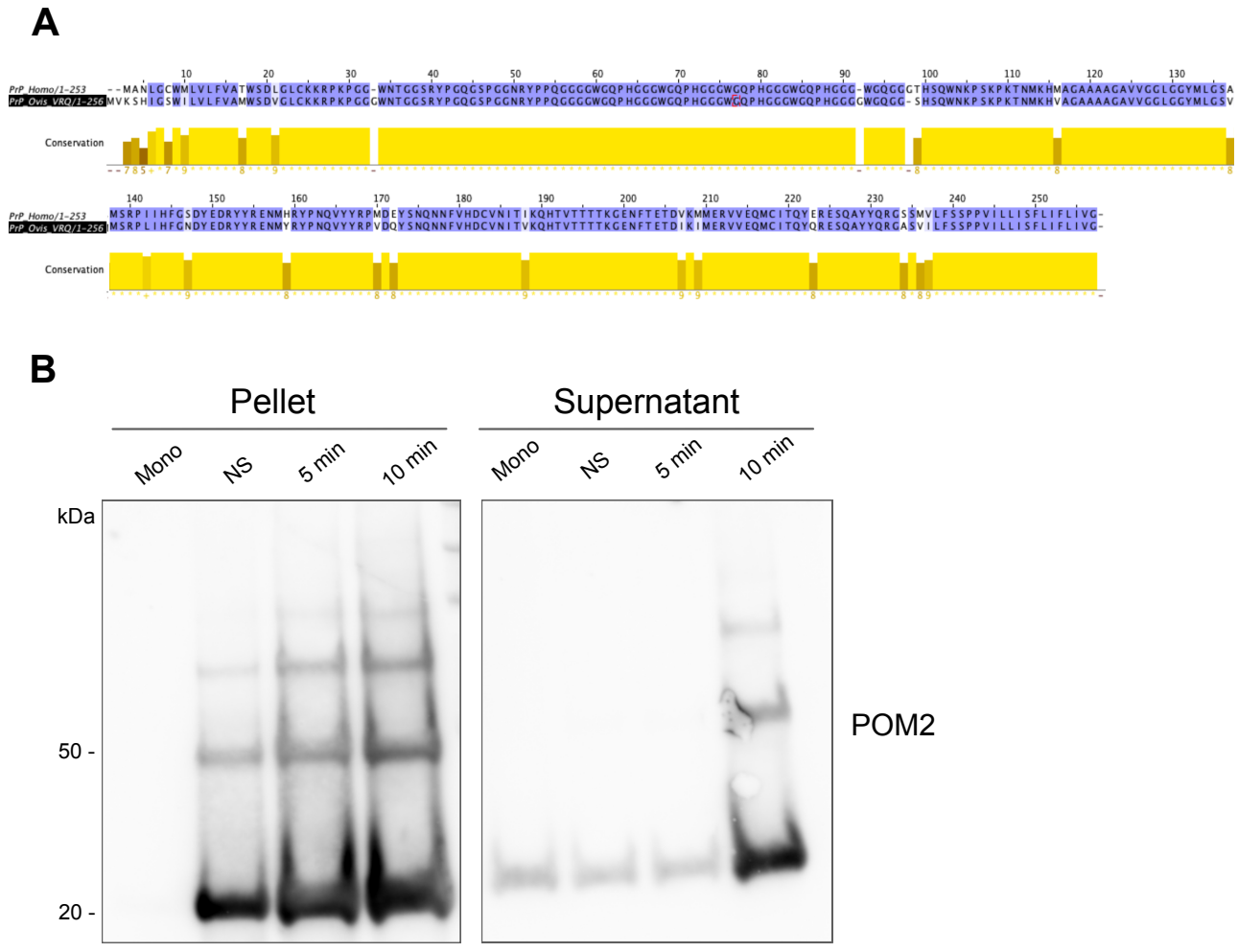


**Supplementary Figure 2. A.** Alignment of the amino acid sequences of the human (top) and sheep (bottom) prion proteins. Residues highlighted in light blue are identical. The alignment was done with Jalview. **B.** Western Blots of pellet and supernatant fractions from a density cushion with 60% iodixanol. Insoluble ovPrP$^{Sc}$ aggregates were present mostly in the pellet fraction. After 10 minutes of sonication, a signal was visible also in the supernatant fraction. Mono: monomeric ovine PrP; NS: ovPrP$^{Sc}$ aggregates not sonicated; 5 min and 10 min: ovPrP$^{Sc}$ aggregates sonicated for 5 min and 10 min, respectively.

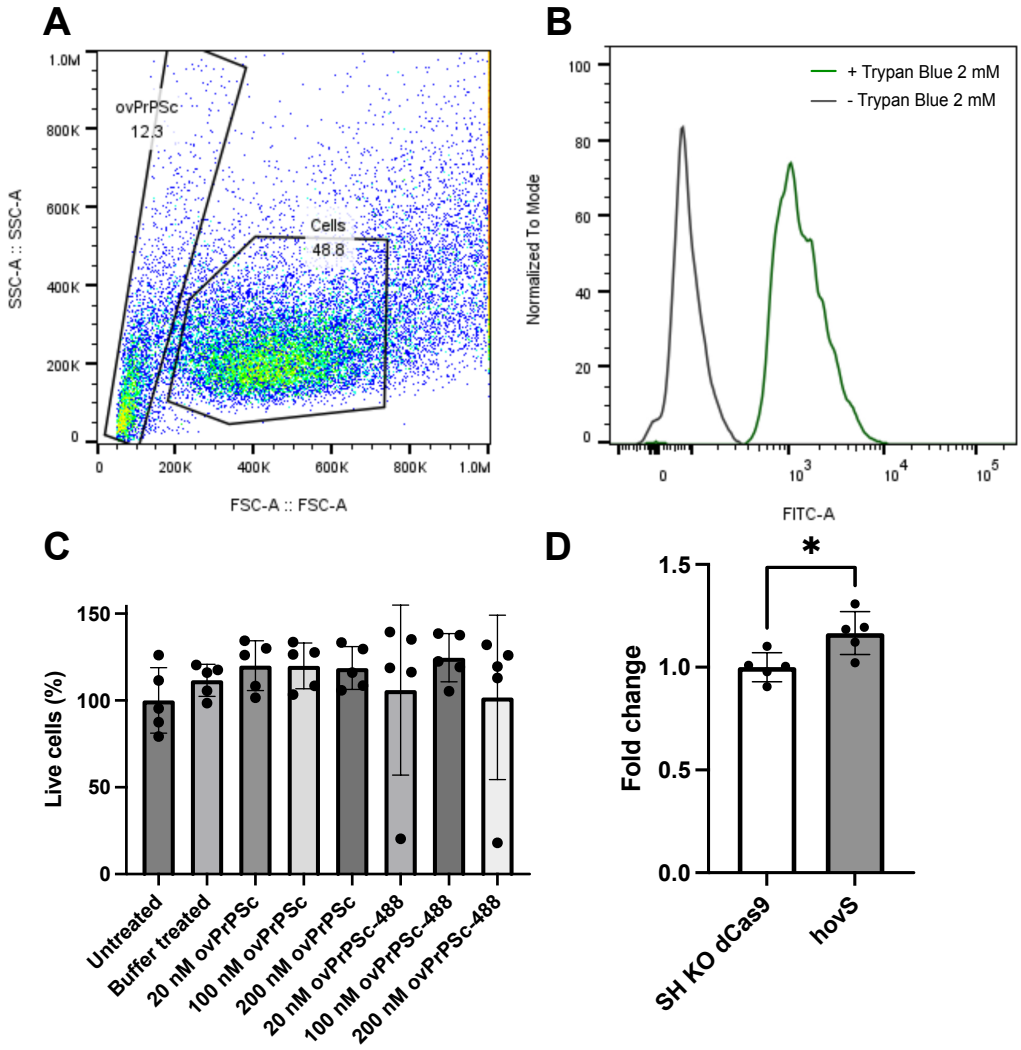


**Supplementary Figure 3. A.** Representative flow cytometry dot plots showing forward scatter area (FSC-A) versus side scatter area (SSC-A) profiles of AF488-ovPrP$^{Sc}$ aggregates and untreated cells. The two samples were mixed immediately before acquisition. **B.** Histogram showing fluorescence intensity of AF488- ovPrP$^{Sc}$ aggregates (X axis, FITC channel) acquired without and with the addition of 2 mM Trypan Blue. Fluorescence intensity decreases almost to zero when Trypan Blue is present in the sample during acquisition. **C.** Viability assay of SH-KO$^{vp649}$ upon incubation with increasing concentrations of ovPrP$^{Sc}$ and AF488-ovPrP$^{Sc}$ aggregates for 24 hours. Results are expressed as percentage of alive cells normalized on the mean of the untreated controls. **D.** Uptake of AF488-ovPrP$^{Sc}$ aggregates in SH-KO$^{vp649}$ cells and in HovS cells overexpressing the sheep prion protein. Data are represented as fold change calculated on the mean of the SH-KO$^{vp649}$ samples. Statistical test: unpaired Student's T test. *: $p<0.05$.

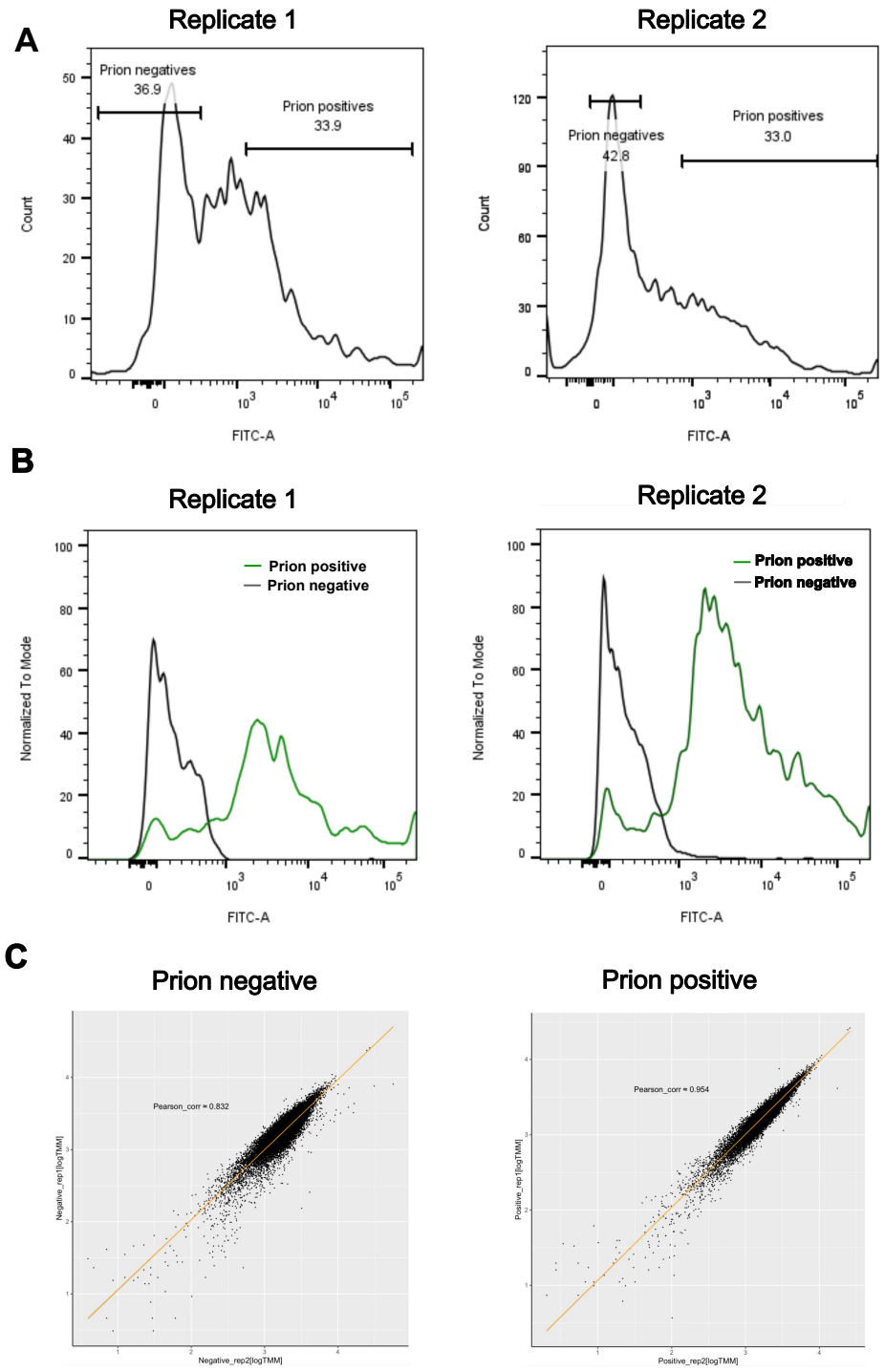


**Supplementary Figure 4. A.** Histogram plots showing the FITC fluorescence intensity profile of the cellular population treated with AF488-ovPrP$^{Sc}$ aggregates for 24 hours, immediately before sorting. The two plots refer to the first (left) and second (right) biological replicate of the primary screen. Horizontal lines represent the two sorted populations. **B.** Reanalysis of the two sorted populations in the first (left) and second (right) biological replicate of the primary screen. **C.** Replicate correlation for the prion negative (left, Pearson corr.:0.83)) and prion positive (right, Pearson corr.:0.95) populations, calculated on NGS read counts.

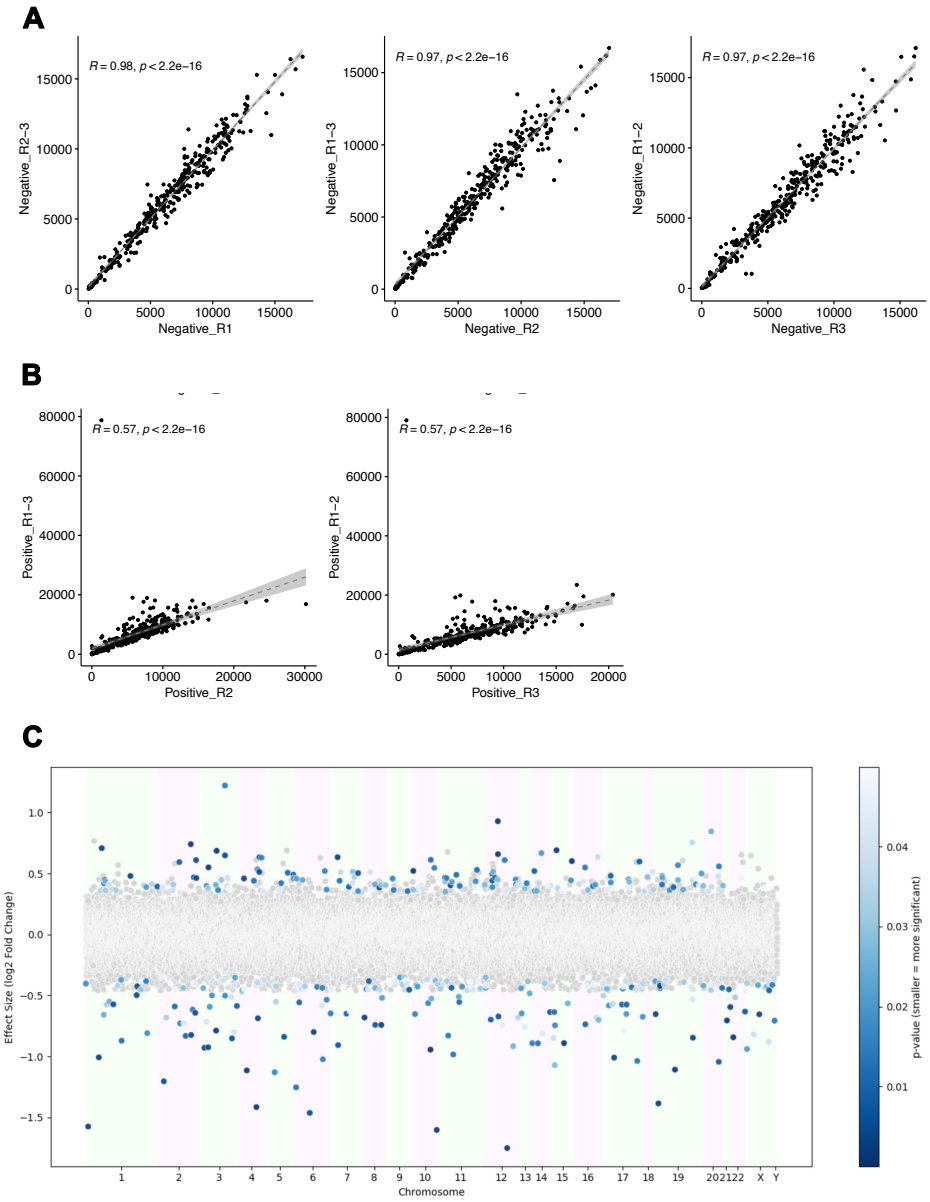


**Supplementary Figure 5.** Correlation analysis of biological replicates for the prion-negative **(A)** and prion-positive **(B)** populations in the secondary screen. Correlations were calculated based on NGS read counts. Each of the three biological replicates was compared with the other two. The prion-positive population from the first replicate showed poor correlation with the other two and was therefore excluded from further analysis. Panel B only shows the two biological replicates that were used in the analysis. **C.** Relationship between the effect of all genes on prion uptake and their genomic coordinates. Each dot represents a single gene plotted according to its genomic position (X axis) and effect on prion uptake (Y axis, $\log_2$ Fold Change). Genes that passed the $\log_2$ fold change and p-value thresholds are highlighted with colors reflecting their p-value.

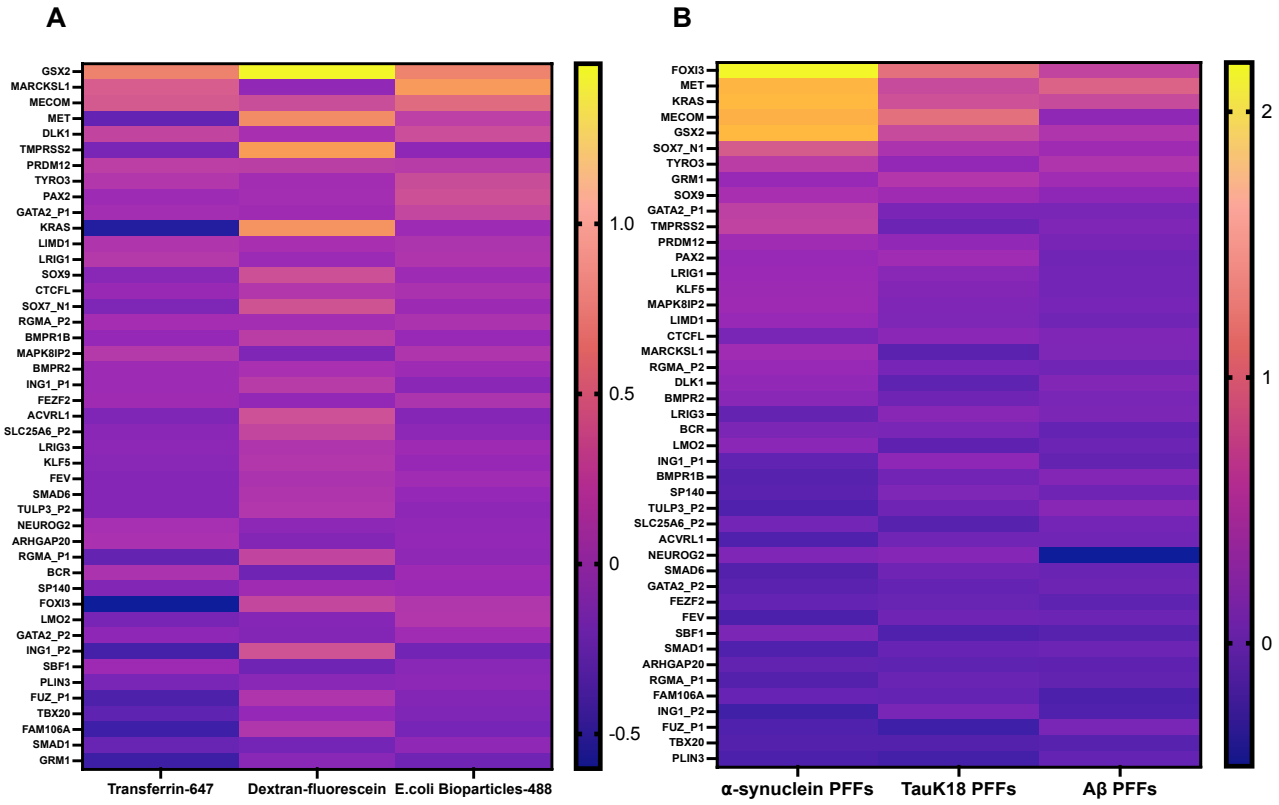


**Supplementary Figure 6.** Heat map showing the $Log_2FC$ of the uptake of non aggregated probes (**A**) and neurodegeneration-related aggregates (**B**) for all confirmed hit genes. $Log_2FC$ was calculated on the pooled mean of 10 non-targeting qgRNA guides, each one assayed in triplicate (total = 30 technical replicates).

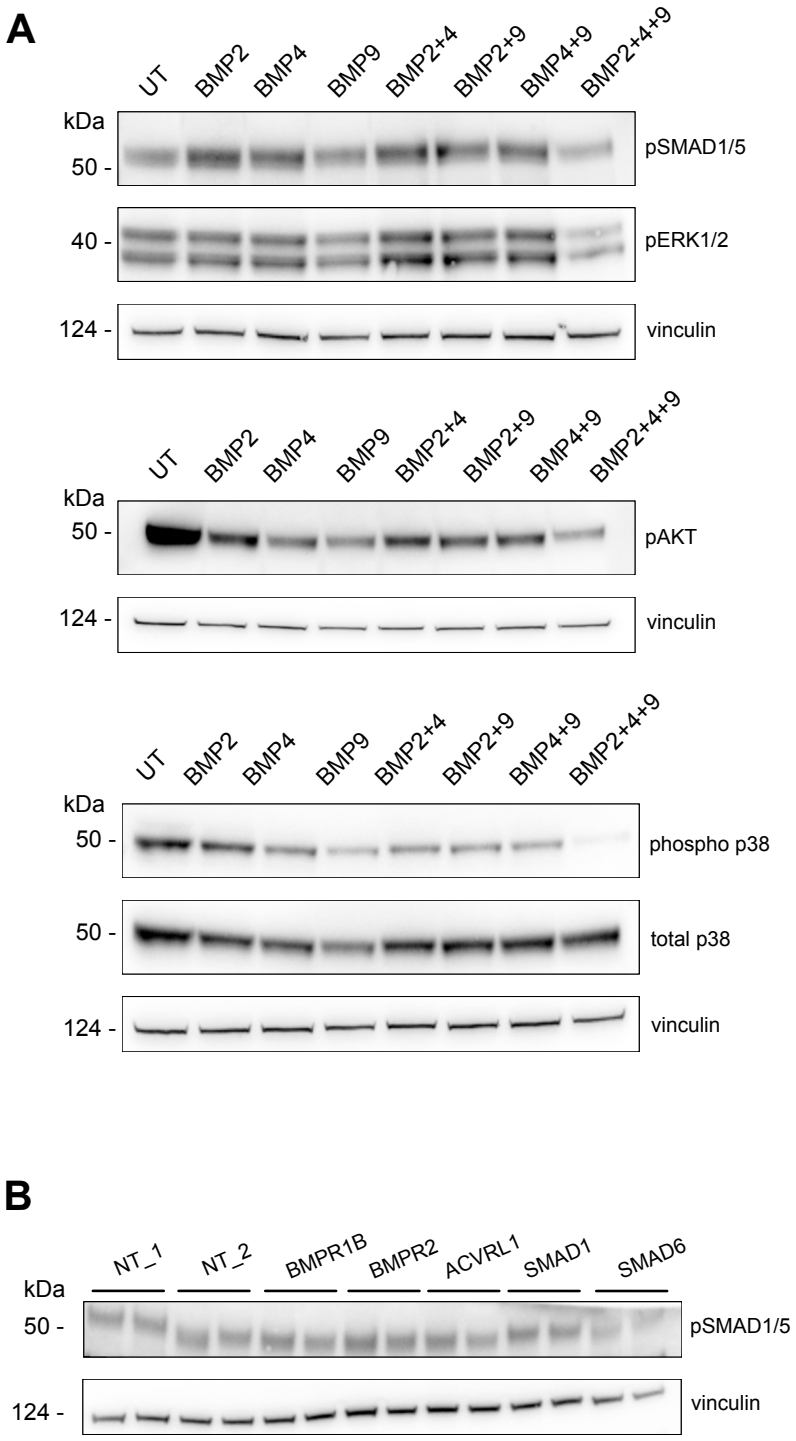


**Supplementary Figure 7. A.** Western Blots of canonical (pSMAD1/5) and non-canonical (pERK1/2, pAKT, phosphor p38/p38) downstream effectors of the BMP pathway in SH-KO$^{vp649}$ cells treated with individual or combinations of BMP peptides at 50 ng/mL for 4 days. UT: untreated control. **B.** Western Blot of canonical (pSMAD1/5) downstream effector of the BMP pathway in SH-KO$^{vp649}$ upon genetic upregulation of individual hit genes. Vinculin was used as loading control.

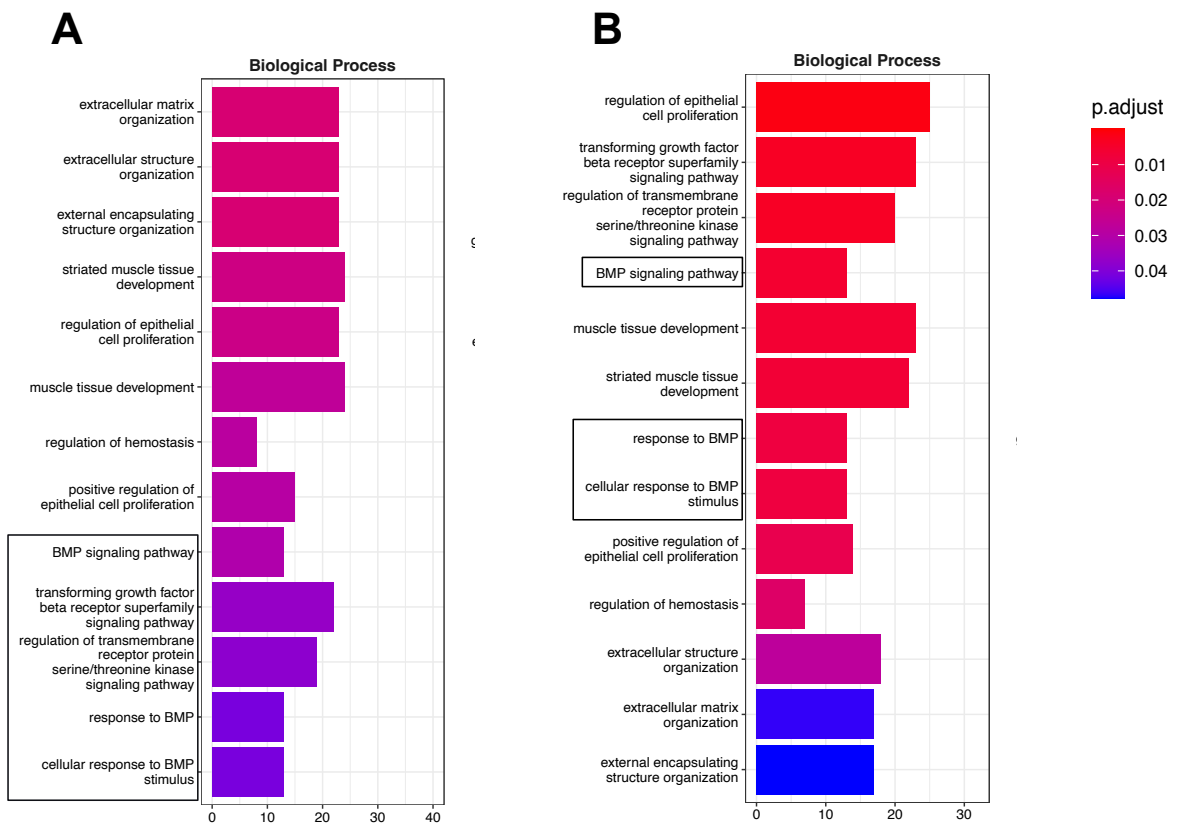


**Supplementary Figure 8.** Gene Ontology analysis reveals enrichment of BMP-related GO terms consistently across the DEG datasets of HovH **(A)** and HovL **(B)** cells.

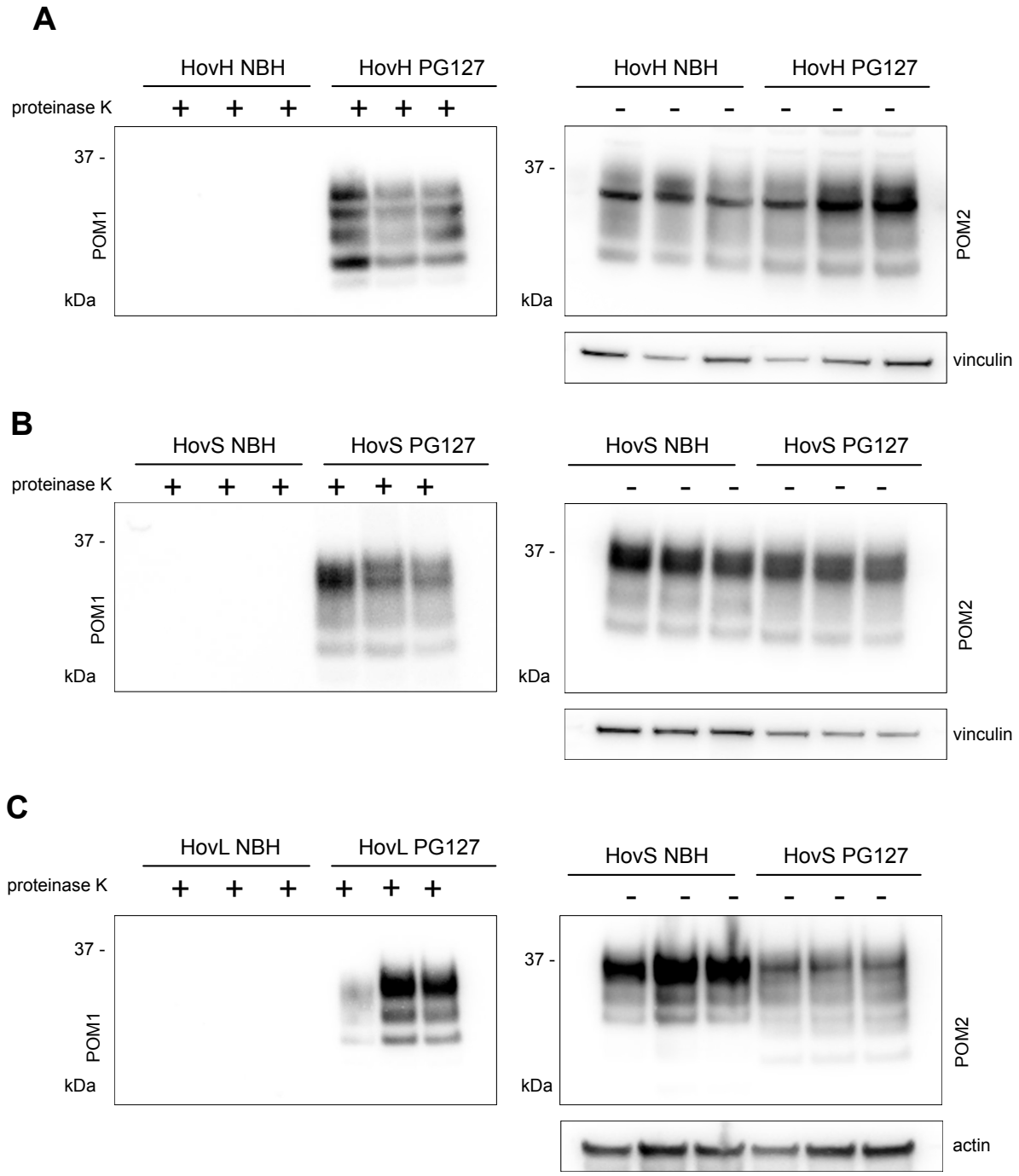


**Supplementary Figure 9.** Western Blots of HovH (**A**), HovS (**B**) and HovL (**C**) cell lines infected either with non-infected (NBH) or prion-infected (PG) brain homogenates. Proteinase K digestion shows the presence of PK-resistant $PrP^{Sc}$ only in the PG-infected cells. Vinculin (**A and B**) and actin (**C**) were used as loading controls.

## Original uncropped, unadjusted blot images

**Figure 1F.** Membrane was cut at 75 kDa. Membrane 1 was incubated with POM1 and membrane 2 with anti-vinculin.

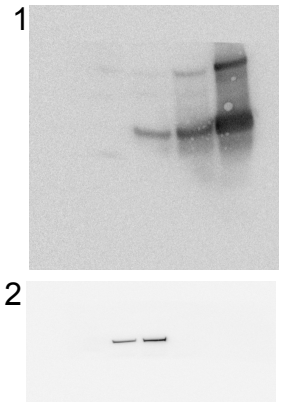


**Figure 5C - HovH.** Membrane was cut at 75 kDa. Membrane 1 was incubated with anti-pSMAD1/5 and membrane 2 with anti-vinculin.

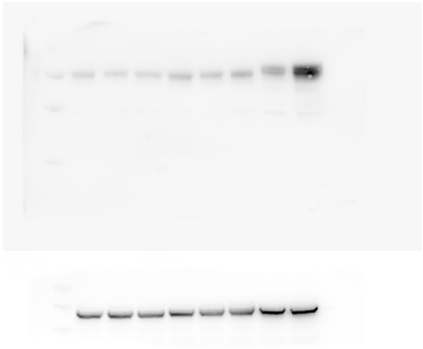

**Figure 5C - HovS.** Membrane was cut at 75 kDa. Membrane 1 was incubated with anti-pSMAD1/5 and membrane 2 with anti-vinculin.

**Figure 5C - HovL.** Membrane was cut at 75 kDa. Membrane 1 was incubated with anti-pSMAD1/5 and membrane 2 was incubated with anti-vinculin.

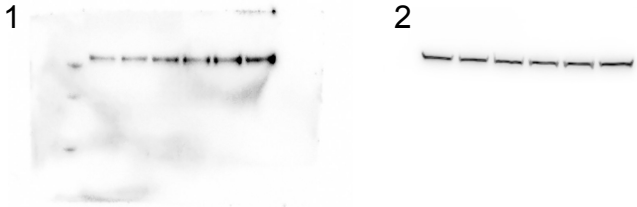


**Uncropped data related to Figure 1F:** Membrane was cut at 75 kDa. Membrane 1 was incubated with POM1 and membrane 2 with anti-vinculin. Figure 5C – HovH: Membrane was cut at 75 kDa. Membrane 1 was incubated with anti-pSMAD1/5 and membrane 2 with anti-vinculin. Figure 5C – HovS: Membrane was cut at 75 kDa. Membrane 1 was incubated with anti-pSMAD1/5 and membrane 2 with anti-vinculin. Figure 5C – HovL: Membrane was cut at 75 kDa. Membrane 1 was incubated with anti-pSMAD1/5 and membrane 2 with anti-vinculin.

**Figure S1A.** Membrane was cut at 75 kDa. Membrane 1 was incubated with anti-Cas9 and membrane 2 with anti-actin HRP

1

2



**Figure S1B.** Membrane was cut at 75 kDa. Membrane 1 was incubated with anti-ADAM10 and membrane 2 with anti-actin HRP

1

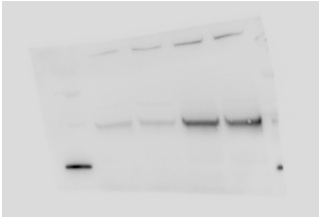

2

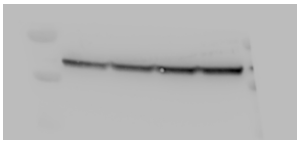

**Figure S1C.** Membrane was cut at 30 kDa. Membrane 1 was incubated with anti-actin HRP and membrane 2 with anti-RAB13

1

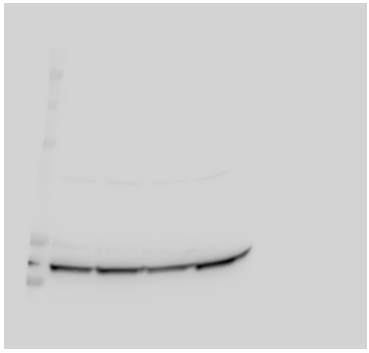

2



**Figure S2B.** Membrane was incubated with POM2

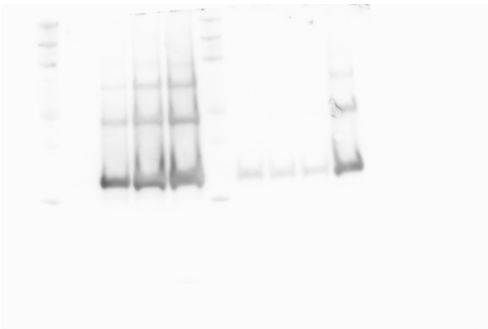

**Uncropped data related to Fig. S1 and S2**

Figure S1A: Membrane was cut at 75 kDa. Membrane 1 was incubated with anti-Cas9 and membrane 2 with anti-actin HRP.

Figure S1B: Membrane was cut at 75 kDa. Membrane 1 was incubated with anti-ADAM10 and membrane 2 with anti-actin HRP.

Figure S1C: Membrane was cut at 30 kDa. Membrane 1 was incubated with anti-actin HRP and membrane 2 with anti-RAB13.

Figure S2B: Membrane was incubated with POM2.

**Figure S7A.** Membranes were cut at 75 kDa. Membranes 1-3-5 were incubated with anti-pERK1/2, anti-pAKT and anti-phospho p38. Membrane 1 was reincubated with anti-pSMAD1/5 without stripping. Membrane 5 was stripped and incubated with anti-p38. Membranes 2-4-6 were incubated with anti-vinculin.

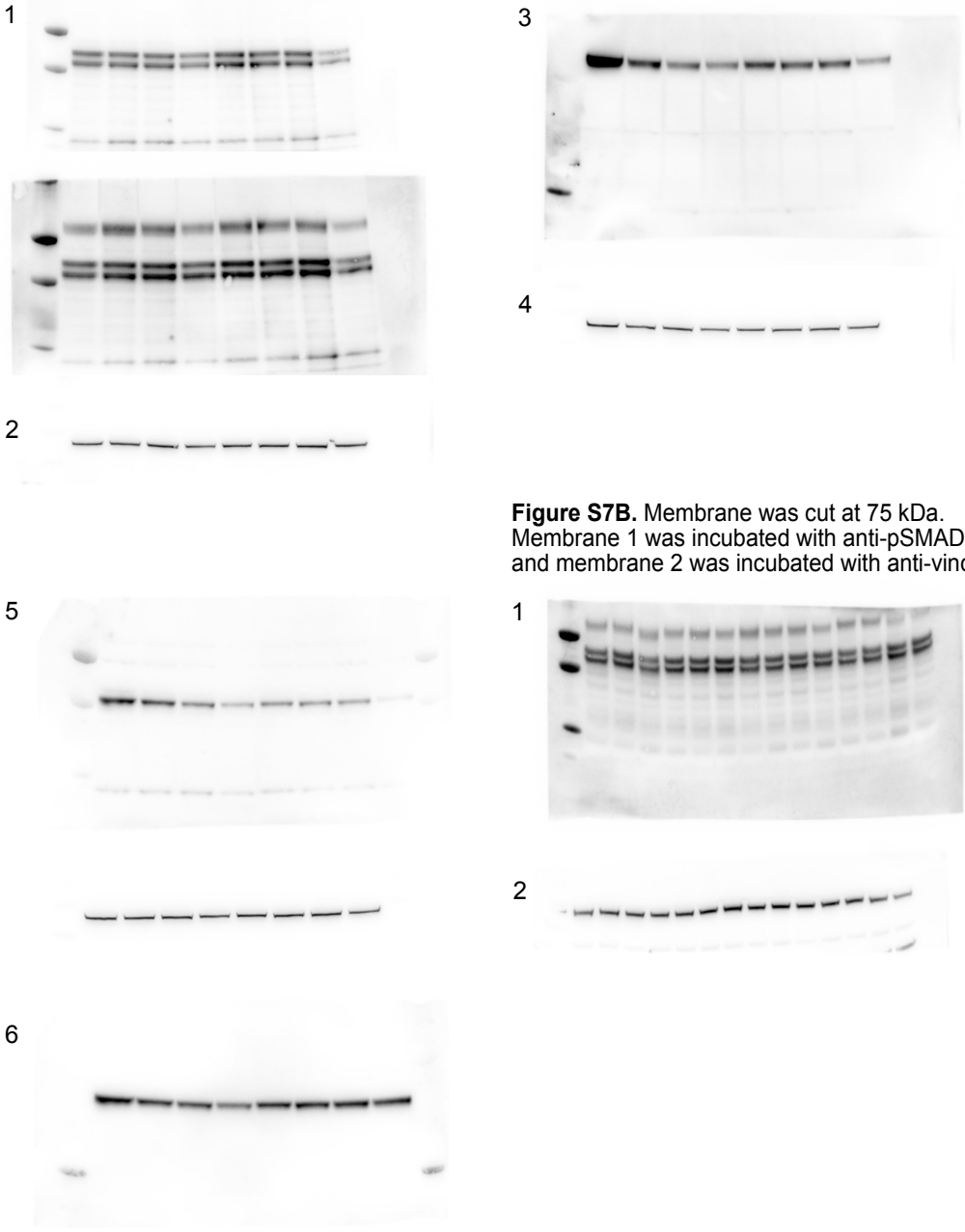


**Figure S7B.** Membrane was cut at 75 kDa. Membrane 1 was incubated with anti-pSMAD1/5 and membrane 2 was incubated with anti-vinculin




**Uncropped data related to Fig S7**

Figure S7A: Membranes were cut at 75 kDa. Membranes 1, 3, and 5 were incubated with anti-pERK1/2, anti-pAKT, and anti-phospho-p38, respectively. Membrane 1 was re-incubated with anti-pSMAD1/5 without stripping. Membrane 5 was stripped and re-incubated with anti-p38. Membranes 2, 4, and 6 were incubated with anti-vinculin.
Figure S7B: Membrane was cut at 75 kDa. Membrane 1 was incubated with anti-pSMAD1/5 and membrane 2 with anti-vinculin.

**Figure S9A.** Membrane 1 was incubated with POM1. Membrane 2 was cut at 75 kDa. Membrane 2 was incubated with POM2 and membrane 3 was incubated with anti-vinculin

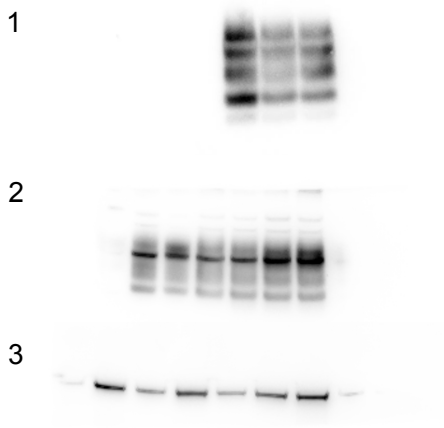


**Figure S9B.** Membrane 1 was incubated with POM1. Membrane 2 was cut at 75 kDa. Membrane 2 was incubated with POM2 and membrane 3 was incubated with anti-vinculin

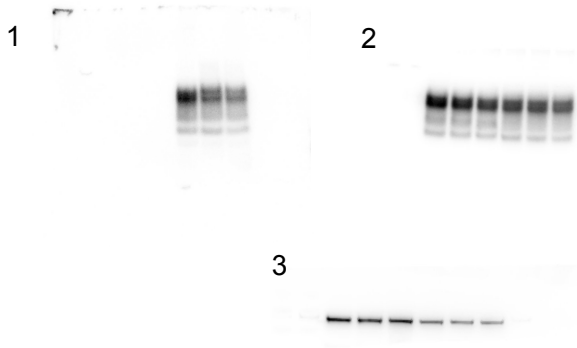


**Figure S9C.** Membrane 1 was incubated with POM1. Membrane 2 was cut at 75 kDa. Membrane 2 was incubated with POM2 and membrane 3 was incubated with anti-vinculin. However, the anti-vinculin antibody did not show any signal and membrane 2 was then incubated with anti-actin HRP without stripping.

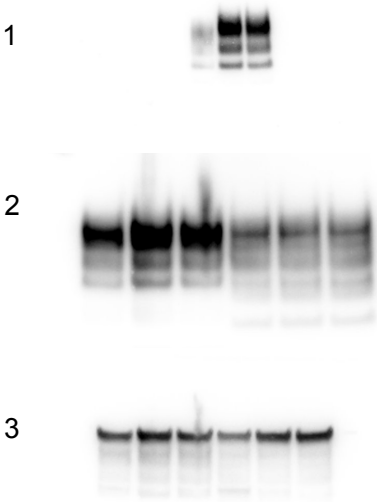


**Uncropped data related to Fig. S9**

Figure S9A: Membrane 1 was incubated with POM1. Membrane 2 was cut at 75 kDa and incubated with POM2. Membrane 3 was incubated with anti-vinculin.

Figure S9B: Membrane 1 was incubated with POM1. Membrane 2 was cut at 75 kDa and incubated with POM2. Membrane 3 was incubated with anti-vinculin.

Figure S9C: Membrane 1 was incubated with POM1. Membrane 2 was cut at 75 kDa and incubated with POM2. Membrane 3 was incubated with anti-vinculin. The anti-vinculin antibody did not show any signal; membrane 2 was therefore incubated with anti-actin HRP without stripping.

**Supplementary Table 1.** Primary hitlist of the genome-wide CRISPR activation screen. Red and blue: positive and negative regulators, respectively.

| *Gene Symbol* | *$log_2$ Ratio* | *pValue* | *directionality* |
|---|---|---|---|
| *NAV3* | -1.75 | 0.001 | DOWN |
| *DOCK1* | -1.60 | 0.001 | DOWN |
| *TP73* | -1.58 | 0.002 | DOWN |
| *CDKN1A* | -1.46 | 0.005 | DOWN |
| *NEUROG2* | -1.42 | 0.000 | DOWN |
| *PLIN3* | -1.39 | 0.001 | DOWN |
| *SSR1* | -1.25 | 0.011 | DOWN |
| *EIF2AK2* | -1.20 | 0.004 | DOWN |
| *RPS23* | -1.13 | 0.015 | DOWN |
| *GSX2* | -1.11 | 0.000 | DOWN |
| *CEBPA* | -1.11 | 0.000 | DOWN |
| *MEIS2* | -1.07 | 0.027 | DOWN |
| *BMP7* | -1.04 | 0.008 | DOWN |
| *OTOP2* | -1.04 | 0.013 | DOWN |
| *SERINC1* | -1.02 | 0.015 | DOWN |
| *KCNJ18* | -1.01 | 0.003 | DOWN |
| *HMGN2* | -1.01 | 0.002 | DOWN |
| *RPS27A* | -0.99 | 0.006 | DOWN |
| *PTPRJ* | -0.98 | 0.012 | DOWN |
| *PAX2* | -0.94 | 0.000 | DOWN |
| *TMSB4X* | -0.94 | 0.020 | DOWN |
| *EOMES* | -0.93 | 0.001 | DOWN |
| *ZDHHC3* | -0.92 | 0.003 | DOWN |
| *MAPKAPK5* | -0.92 | 0.025 | DOWN |
| *LOC105370706* | -0.91 | 0.016 | DOWN |
| *VPS41* | -0.91 | 0.006 | DOWN |
| *PNN* | -0.89 | 0.011 | DOWN |
| *RNASE6* | -0.89 | 0.014 | DOWN |
| *SMAD6* | -0.89 | 0.000 | DOWN |
| *SMIM10L2A* | -0.88 | 0.040 | DOWN |
| *LRIG2* | -0.87 | 0.011 | DOWN |
| *MECOM* | -0.85 | 0.005 | DOWN |
| *OTUD7A* | -0.85 | 0.038 | DOWN |
| *IKZF1* | -0.85 | 0.006 | DOWN |
| *KCNC3* | -0.85 | 0.002 | DOWN |
| *BCR* | -0.84 | 0.000 | DOWN |
| *PCDHB9* | -0.84 | 0.005 | DOWN |
| *METAP1D* | -0.83 | 0.009 | DOWN |
| *GTF2H1* | -0.83 | 0.013 | DOWN |
| *PARD3B* | -0.82 | 0.003 | DOWN |
| *SYP* | -0.82 | 0.039 | DOWN |
| *FAM86C1* | -0.82 | 0.008 | DOWN |
| *FNTB* | -0.81 | 0.043 | DOWN |
| *SRGAP2* | -0.81 | 0.017 | DOWN |
| *ABCC5* | -0.80 | 0.040 | DOWN |
| *RUNX2* | -0.80 | 0.003 | DOWN |
| *FKBP10* | -0.79 | 0.046 | DOWN |
| *FEZF2* | -0.79 | 0.001 | DOWN |
| *LOC105374301* | -0.76 | 0.039 | DOWN |
| *FNDC3A* | -0.76 | 0.044 | DOWN |
| *FSIP1* | -0.75 | 0.015 | DOWN |
| *TRIB1* | -0.74 | 0.002 | DOWN |
| *TPD52* | -0.74 | 0.007 | DOWN |
| *ANKRD52* | -0.74 | 0.044 | DOWN |
| *TUFM* | -0.74 | 0.009 | DOWN |
| *SFT2D3* | -0.73 | 0.015 | DOWN |
| *GRB14* | -0.73 | 0.042 | DOWN |
| *GORASP1* | -0.71 | 0.043 | DOWN |
| *PPP2R3B* | -0.71 | 0.013 | DOWN |
| *TMPRSS2* | -0.71 | 0.000 | DOWN |
| *KARS1* | -0.70 | 0.027 | DOWN |
| *ARHGDIB* | -0.70 | 0.008 | DOWN |
| *LARP1B* | -0.69 | 0.003 | DOWN |
| *CLEC18A* | -0.68 | 0.038 | DOWN |
| *GTF2A1L* | -0.68 | 0.033 | DOWN |
| *SOX7* | -0.68 | 0.001 | DOWN |
| *TMEM132D* | -0.68 | 0.035 | DOWN |
| *HEXD* | -0.67 | 0.018 | DOWN |
| *KRT6A* | -0.67 | 0.005 | DOWN |
| *RSPO1* | -0.66 | 0.024 | DOWN |
| *SLC16A2* | -0.65 | 0.002 | DOWN |
| *AMH* | -0.65 | 0.003 | DOWN |
| *TRDMT1* | -0.65 | 0.015 | DOWN |
| *HDAC5* | -0.65 | 0.019 | DOWN |
| *PON2* | -0.65 | 0.009 | DOWN |
| *KATNAL1* | -0.65 | 0.018 | DOWN |
| *PHF10* | -0.65 | 0.014 | DOWN |
| *SCG2* | -0.64 | 0.004 | DOWN |
| *DLK1* | -0.64 | 0.006 | DOWN |
| *LPCAT4* | -0.64 | 0.011 | DOWN |
| *SBF1* | -0.63 | 0.007 | DOWN |
| *EIF2S1* | -0.63 | 0.022 | DOWN |
| *GBX1* | -0.63 | 0.049 | DOWN |
| *SPDYE6* | -0.63 | 0.048 | DOWN |
| *TMEM169* | -0.62 | 0.013 | DOWN |
| *PRG4* | -0.60 | 0.017 | DOWN |
| *CECR2* | -0.60 | 0.002 | DOWN |
| *DHX30* | -0.59 | 0.019 | DOWN |
| *ZAP70* | -0.59 | 0.010 | DOWN |
| *LRRC15* | -0.59 | 0.008 | DOWN |
| *DSE* | -0.58 | 0.041 | DOWN |
| *TP53* | -0.58 | 0.018 | DOWN |
| *UBTF* | -0.57 | 0.009 | DOWN |
| *KRTAP3-2* | -0.57 | 0.009 | DOWN |
| *CFAP57* | -0.57 | 0.032 | DOWN |
| *GADD45A* | -0.57 | 0.005 | DOWN |
| *FAM106A* | -0.57 | 0.036 | DOWN |
| *VRK2* | -0.57 | 0.048 | DOWN |
| *IREB2* | -0.57 | 0.025 | DOWN |
| *CYP2C9* | -0.56 | 0.015 | DOWN |
| *H3C2* | -0.56 | 0.009 | DOWN |
| *FADS2* | -0.55 | 0.011 | DOWN |
| *LIX1* | -0.55 | 0.034 | DOWN |
| *STIL* | -0.55 | 0.025 | DOWN |
| *GRM1* | -0.54 | 0.015 | DOWN |
| *NUP62* | -0.53 | 0.041 | DOWN |
| *PPRC1* | -0.53 | 0.024 | DOWN |
| *TRPM2* | -0.52 | 0.047 | DOWN |
| *COL22A1* | -0.52 | 0.021 | DOWN |
| *CHEK2* | -0.52 | 0.032 | DOWN |
| *KPNA4* | -0.51 | 0.039 | DOWN |
| *TKFC* | -0.51 | 0.022 | DOWN |
| *SERPINF1* | -0.50 | 0.034 | DOWN |
| *SLC38A3* | -0.50 | 0.018 | DOWN |
| *NECTIN4* | -0.50 | 0.004 | DOWN |
| *ING1* | -0.48 | 0.023 | DOWN |
| *IKBKG* | -0.48 | 0.019 | DOWN |
| *USP17L22* | -0.47 | 0.026 | DOWN |
| *BTNL9* | -0.46 | 0.040 | DOWN |
| *MAPK8IP2* | -0.46 | 0.047 | DOWN |
| *HS3ST1* | -0.46 | 0.026 | DOWN |
| *LOC102723360* | -0.44 | 0.011 | DOWN |
| *SYT15* | 0.38 | 0.043 | UP |
| *RAPH1* | 0.40 | 0.034 | UP |
| *ZNF446* | 0.40 | 0.028 | UP |
| *TMEM126A* | 0.40 | 0.035 | UP |
| *LMO2* | 0.40 | 0.003 | UP |
| *TULP3* | 0.41 | 0.026 | UP |
| *FOXI3* | 0.41 | 0.030 | UP |
| *NFATC3* | 0.41 | 0.020 | UP |
| *KDM2B* | 0.41 | 0.015 | UP |
| *MRPL55* | 0.41 | 0.034 | UP |
| *KLF5* | 0.42 | 0.014 | UP |
| *SMAD5* | 0.42 | 0.012 | UP |
| *TMEM220* | 0.43 | 0.017 | UP |
| *CRYM* | 0.43 | 0.042 | UP |
| *SCMH1* | 0.43 | 0.027 | UP |
| *ARHGAP20* | 0.44 | 0.017 | UP |
| *BMPR1B* | 0.44 | 0.011 | UP |
| *KRAS* | 0.44 | 0.005 | UP |
| *MYCL* | 0.45 | 0.006 | UP |
| *MYL4* | 0.45 | 0.021 | UP |
| *MAK* | 0.46 | 0.021 | UP |
| *RBPJ* | 0.46 | 0.003 | UP |
| *ZNF354B* | 0.46 | 0.021 | UP |
| *TEF* | 0.46 | 0.048 | UP |
| *DKK 3.00* | 0.46 | 0.015 | UP |
| *ZNF426* | 0.47 | 0.024 | UP |
| *ZNF701* | 0.47 | 0.047 | UP |
| *FEV* | 0.47 | 0.007 | UP |
| *COL8A1* | 0.47 | 0.047 | UP |
| *ZNF699* | 0.48 | 0.017 | UP |
| *SCO1* | 0.48 | 0.009 | UP |

| | | | |
|---|---|---|---|
| *ZNF354A* | 0.49 | 0.009 | UP |
| *SOX5* | 0.50 | 0.010 | UP |
| *ZNF17* | 0.50 | 0.020 | UP |
| *TM2D2* | 0.51 | 0.040 | UP |
| *SMAD1* | 0.51 | 0.004 | UP |
| *MET* | 0.51 | 0.028 | UP |
| *IL2RA* | 0.52 | 0.000 | UP |
| *NNMT* | 0.53 | 0.011 | UP |
| *ADAD1* | 0.53 | 0.020 | UP |
| *LIMD1* | 0.55 | 0.000 | UP |
| *CTCFL* | 0.56 | 0.013 | UP |
| *SOX9* | 0.59 | 0.034 | UP |
| *SEC14L1* | 0.60 | 0.006 | UP |
| *PRDM12* | 0.60 | 0.005 | UP |
| *RGMA* | 0.60 | 0.000 | UP |
| *SP140* | 0.61 | 0.004 | UP |
| *LRIG3* | 0.61 | 0.013 | UP |
| *SFXN3* | 0.61 | 0.010 | UP |
| *MARCHF1* | 0.63 | 0.016 | UP |
| *TBX20* | 0.63 | 0.002 | UP |
| *POU4F2* | 0.63 | 0.001 | UP |
| *PMFBP1* | 0.64 | 0.037 | UP |
| *GATA2* | 0.65 | 0.003 | UP |
| *ATG101* | 0.66 | 0.000 | UP |
| *PRKCH* | 0.67 | 0.020 | UP |
| *LRIG1* | 0.69 | 0.000 | UP |
| *TYRO3* | 0.69 | 0.000 | UP |
| *MARCKSL1* | 0.71 | 0.002 | UP |
| *BMPR2* | 0.74 | 0.000 | UP |
| *FUZ* | 0.75 | 0.035 | UP |
| *CDK5RAP1* | 0.84 | 0.025 | UP |
| *ACVRL1* | 0.93 | 0.000 | UP |
| *GATA2* | 1.22 | 0.014 | UP |

**Supplementary Table 2.** Genes confirmed as hits in a secondary screen. Red and blue: positive and negative regulators, respectively. P1, P2, T1 and N1 indicate alternative transcription start sites (TSS) for the same gene.

| *Gene Symbol* | *$log_2$ Ratio* | *P value* | *Positive vs. negative* |
|---|---|---|---|
| ***NEUROG2*** | -1.22E+00 | 2.41E-18 | DOWN |
| ***FEZF2*** | -8.81E-01 | 4.40E-08 | DOWN |
| ***FUZ_P1*** | -7.91E-01 | 1.18E-05 | DOWN |
| ***GSX2*** | -7.91E-01 | 3.06E-02 | DOWN |
| ***PAX2*** | -6.40E-01 | 6.11E-03 | DOWN |
| ***DLK1*** | -6.10E-01 | 1.77E-10 | DOWN |
| ***TMPRSS2*** | -6.06E-01 | 6.71E-04 | DOWN |
| ***SBF1*** | -5.42E-01 | 1.14E-07 | DOWN |
| ***BCR*** | -5.41E-01 | 2.36E-06 | DOWN |
| ***GRM1*** | -4.78E-01 | 5.21E-02 | DOWN |
| ***MECOM*** | -4.57E-01 | 5.80E-02 | DOWN |
| ***SMAD6*** | -3.73E-01 | 1.91E-03 | DOWN |
| ***ATPSCKMT*** | -3.24E-01 | 3.38E-02 | DOWN |
| ***SOX7_N1*** | -3.08E-01 | 2.85E-02 | DOWN |
| ***LRIG3*** | 3.18E-01 | 1.43E-04 | UP |
| ***GATA2_P2*** | 3.20E-01 | 5.73E-02 | UP |
| ***ING1_P1*** | 3.30E-01 | 1.90E-02 | UP |
| ***TBX20*** | 3.49E-01 | 2.13E-03 | UP |
| ***FEV*** | 3.54E-01 | 2.76E-02 | UP |
| ***SLC25A6_P2*** | 3.87E-01 | 4.00E-02 | UP |
| ***SP140*** | 3.83E-01 | 2.83E-03 | UP |
| ***CTCFL*** | 3.91E-01 | 5.73E-04 | UP |
| ***ING1_P2*** | 3.92E-01 | 2.18E-02 | UP |
| ***ACVRL1*** | 3.95E-01 | 4.36E-02 | UP |
| ***PRDM12*** | 4.32E-01 | 1.46E-06 | UP |
| ***KLF5*** | 4.37E-01 | 1.62E-04 | UP |
| ***SLC12A8_T1*** | 4.59E-01 | 9.61E-02 | UP |
| ***BMPR1B*** | 4.65E-01 | 4.92E-04 | UP |
| ***STMN1*** | 4.84E-01 | 9.00E-02 | UP |
| ***TULP3_P2*** | 5.00E-01 | 2.89E-05 | UP |
| ***LIMD1*** | 5.05E-01 | 3.07E-08 | UP |
| ***PLIN3*** | 5.30E-01 | 5.91E-02 | UP |
| ***RGMA_P2*** | 5.54E-01 | 7.40E-07 | UP |
| ***POU4F2*** | 5.94E-01 | 9.78E-02 | UP |
| ***LRIG1*** | 6.07E-01 | 1.15E-05 | UP |
| ***ARHGAP20*** | 6.42E-01 | 2.90E-04 | UP |
| ***BMPR2*** | 7.16E-01 | 1.97E-04 | UP |
| ***TYRO3*** | 7.37E-01 | 1.08E-12 | UP |
| ***MAPK8IP2*** | 7.57E-01 | 5.80E-02 | UP |
| ***GATA2_P1*** | 7.85E-01 | 3.44E-09 | UP |
| ***SOX9*** | 8.62E-01 | 1.96E-11 | UP |
| ***FOXI3*** | 1.23E+00 | 4.28E-05 | UP |
| ***KRAS*** | 1.26E+00 | 2.39E-03 | UP |
| ***MARCKSL1*** | 1.49E+00 | 5.70E-11 | UP |
| ***MET*** | 1.83E+00 | 3.23E-17 | UP |

**Supplementary Table 3.** Chromosomal mapping of confirmed hit genes.

| *hgnc_symbol* | ***C**hromosome **number*** | *start_position* | *end_position* |
|---|---|---|---|
| *STMN1* | 1 | 25884181 | 25907237 |
| *MARCKSL1* | 1 | 32333827 | 32336233 |
| *FOXI3* | 2 | 88446787 | 88452693 |
| *BMPR2* | 2 | 2,02E+08 | 2,03E+08 |
| *FEV* | 2 | 2,19E+08 | 2,19E+08 |
| *SP140* | 2 | 2,3E+08 | 2,3E+08 |
| *LIMD1* | 3 | 45555394 | 45686341 |
| *FEZF2* | 3 | 62369681 | 62374473 |
| *LRIG1* | 3 | 66378794 | 66501263 |
| *SLC12A8* | 3 | 1,25E+08 | 1,25E+08 |
| *GATA2* | 3 | 1,28E+08 | 1,28E+08 |
| *MECOM* | 3 | 1,69E+08 | 1,7E+08 |
| *GSX2* | 4 | 54099523 | 54102498 |
| *BMPR1B* | 4 | 94757937 | 95158448 |
| *NEUROG2* | 4 | 1,13E+08 | 1,13E+08 |
| *POU4F2* | 4 | 1,47E+08 | 1,47E+08 |
| *ATPSCKMT* | 5 | 10225507 | 10249897 |
| *SMAD5* | 5 | 1,36E+08 | 1,36E+08 |
| *GRM1* | 6 | 1,46E+08 | 1,46E+08 |
| *TBX20* | 7 | 35202430 | 35254100 |
| *MET* | 7 | 1,17E+08 | 1,17E+08 |
| *SOX7* | 8 | 10723768 | 10730511 |
| *PRDM12* | 9 | 1,31E+08 | 1,31E+08 |
| *PAX2* | 10 | 1,01E+08 | 1,01E+08 |
| *ARHGAP20* | 11 | 1,11E+08 | 1,11E+08 |
| *TULP3* | 12 | 2877223 | 2941138 |
| *KRAS* | 12 | 25205246 | 25250936 |
| *ACVRL1* | 12 | 51906908 | 51923361 |
| *LRIG3* | 12 | 58872037 | 58920551 |
| *KLF5* | 13 | 73054976 | 73077541 |
| *ING1* | 13 | 1,11E+08 | 1,11E+08 |
| *DLK1* | 14 | 1,01E+08 | 1,01E+08 |
| *TYRO3* | 15 | 41557675 | 41583589 |
| *SMAD6* | 15 | 66702236 | 66782849 |
| *RGMA* | 15 | 93035271 | 93089211 |
| *SOX9* | 17 | 72121020 | 72126416 |
| *PLIN3* | 19 | 4838339 | 4867717 |
| *FUZ* | 19 | 49806866 | 49817376 |
| *CTCFL* | 20 | 57495966 | 57525652 |
| *TMPRSS2* | 21 | 41464296 | 41531116 |
| *BCR* | 22 | 23179704 | 23318037 |
| *SBF1* | 22 | 50443219 | 50483923 |
| *MAPK8IP2* | 22 | 50600677 | 50613981 |
| *SLC25A6* | X | 1386133 | 1392929 |
| *SLC25A6* | Y | 1386133 | 1392929 |

**Supplementary Table 4.** Analysis of arrayed endocytosis screen for non-aggregated probes.

| | **Transferrin-647** | | **Dextran-Fluorescein** | | **Bioparticles-pH Rodo Green** | |
|---|---|---|---|---|---|---|
| **Gene symbol** | $log_2$FC | adj. P-value | $log_2$FC | adj. P-value | $log_2$FC | adj. P-value |
| **SOX9** | -1.32E-01 | 8.83E-01 | 3.17E-01 | 2.07E-01 | -1.29E-02 | >0.9999 |
| **GATA2_P1** | 2.90E-02 | >0.9999 | -2.88E-03 | >0.9999 | 2.44E-01 | 4.62E-01 |
| **FEZF2** | -2.58E-03 | >0.9999 | -7.61E-02 | 9.58E-01 | 8.41E-02 | 9.28E-01 |
| **FOXI3** | -6.02E-01 | 3.41E-02 | 2.57E-01 | 4.63E-01 | 1.06E-01 | 2.54E-01 |
| **KLF5** | -1.38E-01 | 9.64E-01 | 1.20E-01 | 9.25E-01 | -5.81E-02 | >0.9999 |
| **CTCFL** | -4.90E-02 | >0.9999 | 1.19E-01 | 3.48E-01 | 6.96E-02 | 9.96E-01 |
| **TBX20** | -3.56E-01 | 2.06E-01 | -6.62E-02 | 9.98E-01 | -1.83E-01 | 3.11E-01 |
| **SP140** | -1.78E-01 | 9.75E-01 | -2.72E-03 | >0.9999 | -4.00E-02 | >0.9999 |
| **PAX2** | -5.63E-03 | >0.9999 | 2.90E-02 | >0.9999 | 3.18E-01 | 5.80E-01 |
| **FEV** | -1.61E-01 | 9.91E-01 | 7.69E-02 | 9.32E-01 | 5.29E-03 | >0.9999 |
| **SOX7_N1** | -1.99E-01 | 9.87E-01 | 3.44E-01 | <0.0001 | -2.18E-02 | >0.9999 |
| **GSX2** | 7.03E-01 | 2.92E-01 | 1.47E+00 | 9.27E-02 | 7.11E-01 | 9.60E-03 |
| **SMAD1** | -3.08E-01 | 2.06E-01 | -2.47E-01 | 1.92E-01 | -9.75E-02 | 2.03E-01 |
| **GATA2_P2** | -1.05E-01 | 7.98E-01 | -1.69E-01 | 6.71E-01 | 5.34E-04 | >0.9999 |
| **MECOM** | 3.84E-01 | <0.0001 | 2.99E-01 | 5.54E-01 | 5.18E-01 | 1.67E-01 |
| **NEUROG2** | 3.63E-02 | 1.00E+00 | -1.27E-01 | 9.91E-02 | -7.90E-02 | 6.06E-02 |
| **MET** | -3.15E-01 | 1.07E-02 | 7.68E-01 | 2.45E-02 | 1.91E-01 | 7.57E-01 |
| **DLK1** | 2.34E-01 | 5.10E-03 | 4.17E-02 | 9.99E-01 | 3.00E-01 | 3.80E-03 |
| **RGMA_P2** | 2.13E-02 | >0.9999 | 2.55E-02 | >0.9999 | 7.43E-02 | 7.86E-01 |
| **PRDM12** | 1.87E-01 | 5.92E-01 | 1.83E-01 | 5.00E-04 | 1.57E-01 | 2.47E-01 |
| **LRIG1** | 1.30E-01 | 6.04E-01 | -3.29E-02 | >0.9999 | 9.88E-02 | 1.50E-02 |
| **TULP3_P2** | -1.60E-01 | 8.42E-01 | 1.11E-01 | 3.37E-01 | -1.13E-01 | 4.84E-02 |
| **LRIG3** | -1.21E-01 | 9.85E-01 | 9.45E-02 | 4.13E-01 | -1.89E-02 | >0.9999 |
| **RGMA_P1** | -3.26E-01 | 8.61E-01 | 2.32E-01 | 6.76E-01 | -9.50E-02 | 8.93E-01 |
| **GRM1** | -4.93E-01 | 2.33E-02 | -1.36E-01 | 6.34E-02 | -2.70E-01 | 8.25E-02 |
| **TYRO3** | 1.21E-01 | 9.41E-01 | 1.66E-02 | >0.9999 | 2.87E-01 | 4.00E-03 |
| **MARCKSL1** | 4.18E-01 | <0.0001 | -7.99E-02 | 9.90E-01 | 8.65E-01 | 6.10E-03 |
| **SBF1** | -2.11E-02 | >0.9999 | -2.72E-01 | 6.86E-02 | -1.37E-01 | <0.0001 |
| **BCR** | 8.00E-02 | 8.74E-01 | -2.70E-01 | 1.31E-01 | -1.75E-02 | >0.9999 |
| **FUZ_P1** | -4.26E-01 | 8.45E-02 | 1.02E-01 | 9.99E-01 | -1.68E-01 | 3.66E-01 |
| **BMPR2** | -7.29E-03 | >0.9999 | 5.10E-02 | 1.00E+00 | -1.18E-02 | >0.9999 |
| **BMPR1B** | -6.34E-02 | >0.9999 | 1.70E-01 | 3.00E-04 | -5.63E-02 | 8.27E-01 |
| **SLC25A6_P2** | -1.30E-01 | 9.87E-01 | 2.35E-01 | 9.88E-01 | -1.19E-01 | 3.51E-02 |
| **ACVRL1** | -1.85E-01 | 9.38E-01 | 3.24E-01 | 8.57E-01 | -1.51E-01 | 1.85E-01 |
| **MAPK8IP2** | 1.41E-01 | 6.41E-02 | -1.88E-01 | 7.43E-01 | 9.61E-02 | 3.87E-01 |
| **PLIN3** | -2.19E-01 | 5.42E-02 | -1.34E-01 | 9.91E-01 | -1.23E-01 | 4.18E-01 |
| **LIMD1** | 8.95E-02 | 8.73E-01 | 4.56E-02 | >0.9999 | 8.16E-02 | 8.30E-03 |
| **ARHGAP20** | 6.02E-02 | 9.45E-01 | -1.70E-01 | 8.83E-01 | -7.77E-02 | 8.23E-01 |
| **TMPRSS2** | -2.22E-01 | 4.57E-01 | 8.93E-01 | 9.71E-02 | -1.13E-01 | 9.42E-01 |
| **SMAD6** | -1.60E-01 | 9.64E-01 | 1.01E-01 | 7.09E-01 | -7.10E-02 | 9.91E-01 |
| **KRAS** | -5.68E-01 | 1.25E-02 | 8.24E-01 | 2.14E-01 | -8.61E-03 | >0.9999 |
| **FAM106A** | -4.81E-01 | 1.55E-01 | 1.08E-01 | 1.55E-01 | -2.33E-01 | 3.33E-01 |
| **ING1_P1** | -1.20E-02 | >0.9999 | 1.68E-01 | 3.83E-02 | -1.28E-01 | 4.29E-01 |
| **ING1_P2** | -4.63E-01 | 6.49E-01 | 3.38E-01 | 8.90E-01 | -2.57E-01 | 1.85E-01 |
| **LMO2** | -2.30E-01 | 7.63E-01 | -1.47E-01 | 5.88E-01 | 1.18E-01 | 6.16E-01 |

**Supplementary Table 5.** Analysis of arrayed endocytosis screen for neurodegeneration-related aggregates.

| | α-synuclein PFFs | | TauK18 PFFs | | Aβ PFFs | |
|---|---|---|---|---|---|---|
| **Gene symbol** | **$log_2FC$** | **Adj. P-value** | **$log_2FC$** | **Adj. P-value** | **$log_2FC$** | **Adj. p-value** |
| SOX9 | 0.36 | 0.00 | 0.30 | 0.14 | 0.36 | 1.00 |
| GATA2_P1 | 0.57 | 0.13 | 0.03 | 1.00 | 0.57 | 0.61 |
| FEZF2 | -0.11 | 0.99 | -0.08 | 0.99 | -0.11 | 0.05 |
| FOXI3 | 2.18 | 0.04 | 1.02 | <0.0001 | 2.18 | 0.02 |
| KLF5 | 0.28 | 0.21 | 0.09 | 0.52 | 0.28 | >0.9999 |
| CTCFL | 0.03 | >0.9999 | 0.14 | 0.79 | 0.03 | 0.69 |
| TBX20 | -0.21 | 0.35 | -0.20 | 0.37 | -0.21 | 0.01 |
| SP140 | -0.16 | 1.00 | 0.05 | 0.94 | -0.16 | 0.57 |
| PAX2 | 0.23 | 0.55 | 0.31 | 0.42 | 0.23 | >0.9999 |
| FEV | -0.25 | 0.44 | -0.04 | >0.9999 | -0.25 | 0.02 |
| SOX7_N1 | 0.82 | 0.06 | 0.40 | 0.27 | 0.82 | 0.14 |
| GSX2 | 1.69 | 0.01 | 0.65 | 0.93 | 1.69 | 0.00 |
| SMAD1 | -0.22 | 0.94 | -0.09 | 0.98 | -0.22 | 0.38 |
| GATA2_P2 | -0.17 | 0.97 | -0.10 | 0.95 | -0.17 | 0.35 |
| MECOM | 1.62 | 0.00 | 1.03 | 0.01 | 1.62 | <0.0001 |
| NEUROG2 | 0.07 | 0.98 | 0.11 | 0.99 | 0.07 | >0.9999 |
| MET | 1.66 | <0.0001 | 0.65 | 0.00 | 1.66 | 0.56 |
| DLK1 | 0.20 | 0.34 | -0.15 | 0.96 | 0.20 | >0.9999 |
| RGMA_P2 | 0.24 | 0.38 | 0.00 | >0.9999 | 0.24 | 0.79 |
| PRDM12 | 0.31 | 0.06 | 0.19 | 0.32 | 0.31 | >0.9999 |
| LRIG1 | 0.25 | 0.25 | 0.13 | 0.99 | 0.25 | 0.98 |
| TULP3_P2 | -0.23 | 0.78 | -0.04 | >0.9999 | -0.23 | 0.93 |
| LRIG3 | -0.11 | 1.00 | 0.12 | 0.68 | -0.11 | 0.01 |
| RGMA_P1 | -0.21 | 0.98 | -0.08 | >0.9999 | -0.21 | 0.40 |
| GRM1 | 0.23 | 0.74 | 0.46 | <0.0001 | 0.23 | 0.52 |
| TYRO3 | 0.53 | 0.18 | 0.21 | 0.45 | 0.53 | 0.98 |
| MARCKSL1 | 0.31 | 0.52 | -0.16 | 0.00 | 0.31 | 0.62 |
| SBF1 | 0.04 | >0.9999 | -0.22 | 0.03 | 0.04 | >0.9999 |
| BCR | 0.04 | 1.00 | 0.02 | >0.9999 | 0.04 | >0.9999 |
| FUZ_P1 | -0.23 | 0.41 | -0.31 | 0.06 | -0.23 | >0.9999 |
| BMPR2 | 0.14 | 0.99 | -0.05 | >0.9999 | 0.14 | 0.99 |
| BMPR1B | -0.18 | 0.96 | -0.03 | >0.9999 | -0.18 | 1.00 |
| SLC25A6_P2 | -0.02 | >0.9999 | -0.18 | 1.00 | -0.02 | 1.00 |
| ACVRL1 | -0.23 | 0.98 | -0.03 | >0.9999 | -0.23 | 0.49 |
| MAPK8IP2 | 0.28 | 0.46 | 0.07 | 0.64 | 0.14 | 1.00 |
| PLIN3 | -0.24 | 0.50 | -0.29 | 0.03 | 0.04 | 1.00 |
| LIMD1 | 0.24 | 0.09 | 0.05 | 0.98 | 0.11 | 0.99 |
| ARHGAP20 | -0.12 | 0.99 | -0.14 | 1.00 | 0.00 | 0.37 |
| TMPRSS2 | 0.58 | 0.03 | -0.07 | 1.00 | 0.21 | 1.00 |
| SMAD6 | -0.20 | 0.95 | -0.05 | >0.9999 | 0.07 | 0.96 |
| KRAS | 1.70 | 0.07 | 0.72 | 0.02 | 0.80 | 0.43 |
| FAM106A | -0.09 | >0.9999 | -0.10 | 0.85 | -0.10 | 0.27 |
| ING1_P1 | -0.13 | >0.9999 | 0.16 | 0.90 | 0.03 | 1.00 |
| ING1_P2 | -0.29 | 0.94 | 0.03 | >0.9999 | -0.09 | 0.76 |
| LMO2 | 0.14 | 0.96 | -0.14 | 0.73 | 0.08 | 0.56 |